LINKAGES BETWEEN FLUID FLOW PATHS, REACTIVE GASES, AND CHEMICAL WEATHERING ACROSS A SHALE BEDROCK HILLSLOPE

BY

JIA WANG

THESIS

Submitted in partial fulfillment of the requirements
for the degree of Master of Science in Geology
in the Graduate College of the
University of Illinois at Urbana-Champaign, 2019

Urbana, Illinois

Adviser:

Assistant Professor Jennifer Druhan
Professor Thomas Johnson

ABSTRACT

While the vadose zone is hypothesized to be an active region of solute generation, direct observations to verify this is lacking. Here, we report an integrated approach to characterize chemical weathering reactions in the vadose zone using a novel Vadose Monitoring System (VMS) installed at the Eel River CZO in combination with laboratory experiments and reactive transport modeling. The VMS allows for the direct observation of chemical and gas signatures in the vadose zone for the comparison of chemical evolution of fluids in lab experimental setting. We sampled water and gases across 18 meters of thick regolith at high spatiotemporal resolution over two years, observing a dynamic range of major cation concentrations and ion ratios that vary primarily with depth rather than time despite large seasonal changes in water storage. To validate our simulations, we combine direct observations of solute chemistry from the VMS with the results of batch dissolution experiments using bedrock samples collected from a range of depths across the weathering profile. Using a set of reactive transport models, we evaluate the extent to which these coupled water-gas-rock reactions drive weathering and the observed solute fluxes across a lithological gradient of regolith. Our unique reactive transport model shows that this subtle difference of changing regolith material through depth is crucial to accurately predicting the evolution of solute fluxes. Furthermore, our model results suggest that effective flow rate for the yearly resolution is not the principle factor governing solute concentrations. In total, our work shows that the influence of chemical reactivity across this gradient of weathered solid is a nuance important to accurately portraying solute fluxes from across the profile of the vadose zone.

ACKNOWLEDGEMENTS

This research would not be possible without the support from my family, friends, and colleagues. Thanks to Gideon Bartov, Naomi Wasserman, and Nicole Fernandez for their mentorship and help on the iCAP-Q. I would like to thank Dr. Jennifer Druhan and Dr. Daniella Rempe for their support in completing this project. I would like to particularly thank Mahta Ansari and Paul Ginsberg who were there to help me reason through thoughts to help me make difficult decisions. Thank you to Cecilia for being my roommate for the last two years and keeping me sane.

TABLE OF CONTENTS

CHAPTER 1: MOTIVATION AND BACKGROUND

1.1 Chemical weathering

Chemical weathering and hydrological transport are important components of the cycle by which carbon and other reactive elements are moved and stored through the earth's land, oceans, and atmosphere. In particular, such transport and transformation of common crustal materials cycles carbon from the atmosphere into the oceans. An estimated 0.163 (Dessert et al., 2003) and 0.148 (Gaillardet et al., 1999) gigatons of carbon per year (GtC/yr) are removed from the atmosphere due to the dissolution of silicates and carbonates, respectively. Given the significance of this pathway, it is imperative to quantify chemical weathering rates within these hotspot regions on the Earth's surface and predict the ways in which these systems will adjust to changes in hydrologic cycles and increasingly warming climate.

Environmental systems which host and sustain high rates of chemical weathering must support a high supply rate of fresh bedrock available for dissolution (e.g. from tectonic uplift), actively draining hydrologic flow paths for fluid and solute transport (e.g. hillslopes), and the presence of reactants such as CO_2 and O_2 gasses (e.g. partially saturated systems). These components are common to virtually all upland vadose zones (the unsaturated section of the subsurface from the active soil horizon(s) to the top of the saturated groundwater table) and many recent studies have suggested these systems provide ideal conditions for elevated chemical weathering rates (Brantley et al., 2007; Rempe & Dietrich, 2018; White et al., 2015). Such inferences of high reactivity in the vadose zone are largely based on distinctive differences between solute signatures of dilute soil waters and more concentrated groundwater and streams, suggesting a significant gain in solute content occurring as water drains through the vadose zone. While these observations point to the importance of chemical weathering in the vadose zone, direct geochemical observations confirming high vadose zone reaction rates are largely unavailable, principally due to challenges inherent in sampling across deep unsaturated regolith.

1.2 Fluid pathways through the vadose zone

A quantitative description of the chemical reactions occurring as fluid drains through the vadose zone requires the characterization of both water-rock interactions and the pathways through which water, solutes and gases are transported. The principal mechanism of groundwater recharge in hillslopes is accomplished through fluid flowing preferentially via the fractures of weathered

bedrock, as well as from fluid held in pores of regolith matrix blocks (Manna et al., 2017; Sukhija et al., 2003; Xiang et al., 2019). Water residence time is commonly assumed to be an important regulator of the extent to which chemical reactions may progress (Dellinger et al., 2015; Jung & Navarre-Sitchler, 2018; Maher, 2011; Pogge von Strandmann et al., 2014; Shand et al., 2005). At slow flow rate, fluid is expected to have a long residence time and thus allow chemical reactions to proceed further towards thermodynamic equilibrium and impart a higher fluid solute signature. At high flow rate, fluid is expected to be further away from thermodynamic equilibrium with the mineral surfaces, resulting in a lower solute signature. While these factors are important, it is difficult to parse out the relative contributions to solute generation from fracture vs matrix fluid interactions. This is particularly challenging to constrain within the vadose zone, where data are difficult to collect and these influences have only been inferred based on soil water and groundwater samples. For example, in a 7 day continuous sprinkler experiment conducted at Mettman Ridge in the Oregon Coast Range, fluid samples were collected from lysimeters installed in colluvium and saprolites across the upper 1.5 meters of regolith (Anderson & Dietrich 2001) and two weirs located down gradient from the sprinklers were used to measure discharge rate and runoff chemistry of fluids. They found that under hydrologic steady state (from the continuous application of water), soils were only responsible for approximately ~50% of the total dissolved solids in water draining through the weirs. This implies that approximately 50% of solutes observed in groundwater and streams are generated within the weathered bedrock zone, where the least information (hydrologic and chemical) is available.

The role of this sub-soil fluid reservoir as a vital source for ecosystem sustainability is now emerging in the literature, often termed ‘rock moisture’, as an analog to water stored as soil moisture, but hosted deeper in the vertical profile above the water table (Rempe & Dietrich, 2014). However, rock moisture is not just deeper soil moisture, and in fact the seasonal dynamics of this reservoir appear to be quite unique. For example, a multi-year monitoring study by Salve et al. (2012) and subsequent work from Rempe & Dietrich (2018) in the upland hillslopes of the Eel River drainage network in Mendocino County California have shown that the first rains of the wet season increase rock moisture held in the vadose zone rather than raise the elevation of the groundwater table. Critically, this implies that changes in rock moisture storage are not necessarily detectable in the response of the groundwater table to precipitation events and are thus easily overlooked in the larger hydrologic system until moisture capacity is reached and the system opens

up flow paths to the underlying aquifer. This observation in turn suggests that fluid residence time is partly a function of the retention threshold of the weathered bedrock and that fluid at various times of the year (i.e. dry vs wet season) may have different residence times, and thus different solute compositions, above the water table.

The question then becomes: through what reactive pathways and under what transport controls are these solutes generated? Consider an upland hillslope system, where the groundwater recharge is reasonably assumed to be water flowing vertically downward from soil to bedrock until it reaches the water table, below which lateral flow may also occur. When we sample groundwater, we assume that the solute signature measured is reflecting the balance between the rate at which infiltrating fluid was transported to that location in the and the water-rock interactions that occurred over that distance (i.e. how fast water moved through the near surface to reach the aquifer, and which chemical reactions occurred along the way). Yet if one assumes that the solute concentrations merely reflect the mean residence time of the fluid flow rate within the unsaturated zone, this is a highly simplified representation that does not capture the nuances of rock moisture storage described in the transport pathway above.

Further, a simple conceptual model of Earth surface weathering depicts the most weathered material (i.e. soils) on the surface and the least weathered material (i.e. fresh coherent bedrock) deep into the subsurface (Anderson et al., 2007). Thus, fluid infiltrating through these systems encounters regolith sequentially from most weathered (soil) to least weathered (fresh bedrock) as it progresses along the flow path. The solute signature of fluids which have navigated this weathering gradient therefore should not be expected to reflect water-rock interactions characteristic of exposure to a single material (e.g. parent bedrock or weathered soils). Instead, they represent a history of reaction over the complete sequence of variably weathered materials encountered by the fluid. From this perspective, solute concentrations at depth (e.g. in aquifers and baseflow of streams) reflects the integration of a sequential set of lithology and associated chemical reactions, along with a diversity of residence times. This concept is distinctly different from the perspective of mean fluid residence time across the weathering zone, where transport dictates the extent to which fluid and rock are equilibrated.

1.3 Approach

In total, the poorly constrained role of vadose zone solute generation in our current conceptual understanding of weathering highlights the need for direct observations linking transport and chemical processes within the highly dynamic and reactive depth interval between the base of soils and the groundwater table. Many studies have developed numerical and analytical models constrained by the physical measurements and chemical compositions of saturated groundwater and nearby streams to predict the behavior of weathering and transport through the vadose zone (Banks et al., 2009; Mayer et al., 2002; Reis & Brantley, 2017). Previous studies have attempted to use empirical relationships, observable physical parameters, and laboratory experiments to constrain hydrodynamic transport and chemical weathering processes (Fletcher et al., 2006; Reis & Brantley, 2017) without the means to validate these inferences via direct observations.

A common means of constraining the relative effects of transport and chemical reactions is by isolating water-rock interactions from fluid transport effects through discrete batch reactor experiments using solids recovered from the subsurface (Alekseyev, Medvedeva, Prisyagina, & Balabin, 1997; Van Cappellen, Dixit, & van Beusekom, 2002). Such experiments are often used to constrain dissolution and secondary precipitation rates of minerals by monitoring the concentration of solutes in fluid over time in a well-mixed and closed environment. An extension of such traditional batch reactor experiments is to use mineral surface imaging techniques such as Scanning Electron Microscope (SEM) to quantify the extent to which mineral dissolution and precipitation penetrated the surface of rock samples after the experiments (Harrison et al., 2017; Jew et al., 2017). Such experiments are beyond the scope of the current study but may further elucidate how weathering occurs on mineral surfaces within the vadose zone.

While a single batch reactor experiment using either a depth-integrated or single grab sample of solid material provides a robust method to constrain mineral reaction rates for that specific mineral assemblage, this approach cannot capture fluid evolution through a weathering gradient from soil to groundwater. In this sense, the role of fluid transport across the vadose zone becomes a set of physical pathways through which fluids evolve as a result of a series of water-rock interactions due to varying solid composition. This leads to a testable hypothesis: The evolution of fluid solute chemistry across a natural weathering profile is influenced by the

distinctive depth-varying solid composition along the transport pathway and this nuance cannot be captured simply by mixing a series of solids recovered from the same profile.

The principle purpose of the present study is to leverage a novel sampling system installed across a partially weathered vadose zone sequence to obtain direct observations of solute concentrations in regolith fluid. Using this set of direct observations in conjunction with a series of depth–resolved batch reaction studies and numerical simulations of reactive transport across the soil to bedrock weathering gradient, we aim to deconvolve the effects of transport pathways and this sequential reactivity on the resulting solute composition of fluids draining the Critical Zone.

CHAPTER 2: FIELD SITE

We report a set of high resolution spatiotemporal geochemical datasets from a vadose zone weathering profile using a novel instrumentation and sampling capability installed in October of 2015 on a steep (average 32°) hillslope (39.729 N, 123.644 W) located in the Angelo Coast Range Reserve in Northern Mendocino County California. This site is the principle location of the Eel River Critical Zone Observatory (ER-CZO) (Figure 1A). The geology in this area is structurally complex, largely due to its proximity to the Mendocino triple junction, where the Gorda, North American, and Pacific Ocean plates converge (McLaughlin, 2000). The site is underlain by the Yager terrane of the Coastal Belt of the Franciscan Formation, composed of tectonically folded mudstone dominated by turbidite sequences and interbedded with lenses of sandstone and conglomerate (Blake Jr et al., 1985). The bedrock is composed of a primary mineral assemblage typical for clay-rich shales: quartz (~24.8%), albite (~21.9%), chlorite (~18.3%), illite (~7.4%), smectite (~12.6%), kaolinite (~3.5%), and carbonate (~2.2%) based on XRD analyses. Active uplift in the area sustains an erosion rate of ~0.2 to 0.4 mm/year (Fuller et al., 2009). The ER-CZO is ideally suited for this study because it is composed of a well-developed bedrock weathering profile ranging 5 to 25 meters deep from the base to the ridge of the hillslope, resulting in a thick vadose zone (matrix rock porosity from 3-10%) overlain by thin soil. The site receives an average precipitation of ~1900 mm annually (Salve et al., 2012) which is divided into seasonal cycles of cold wet winter and dry warm summer. Most precipitation occurs between October and May.

CHAPTER 3: METHODS

3.1 VMS and field sampling

A uniquely designed system for vadose zone fluid and gas sampling was installed in the hillslope in October of 2015, hereafter referred to as the Vadose zone Monitoring System (VMS). The VMS consists of two sub-horizontally drilled boreholes hosting a set of parallel flexible sleeves (referred to as VMS-A and VMS-B) ~1 meter apart from each other (Fig. 1B). VMS-A is instrumented with 10 pressure-controlled lysimeter samplers ranging from 1.9 meters to 16.5 meters into the vadose zone with 0.25 m long fine quartz sand silica pillows (grain size <50μm) at each port to provide a means for fluid to continuously flow from outer coarser material into the port. VMS-B is instrumented with 10 free drainage samplers from 1.4 to 15.3 meters where a 1.5-meter-long trough drains to 0.25 long silica pillows to filter water draining into each sampler cup. TDT moisture sensors are instrumented along VMS-A and gas ports to monitor pCO_2 and pO_2 are instrumented along VMS-B. A control panel above ground is used for sample collection. Using the novel capabilities of the VMS, Druhan et al. (2017) reported the first direct observations of solute generation in the partially saturated, fractured saprolite comprising the vadose zone of the ER-CZO.

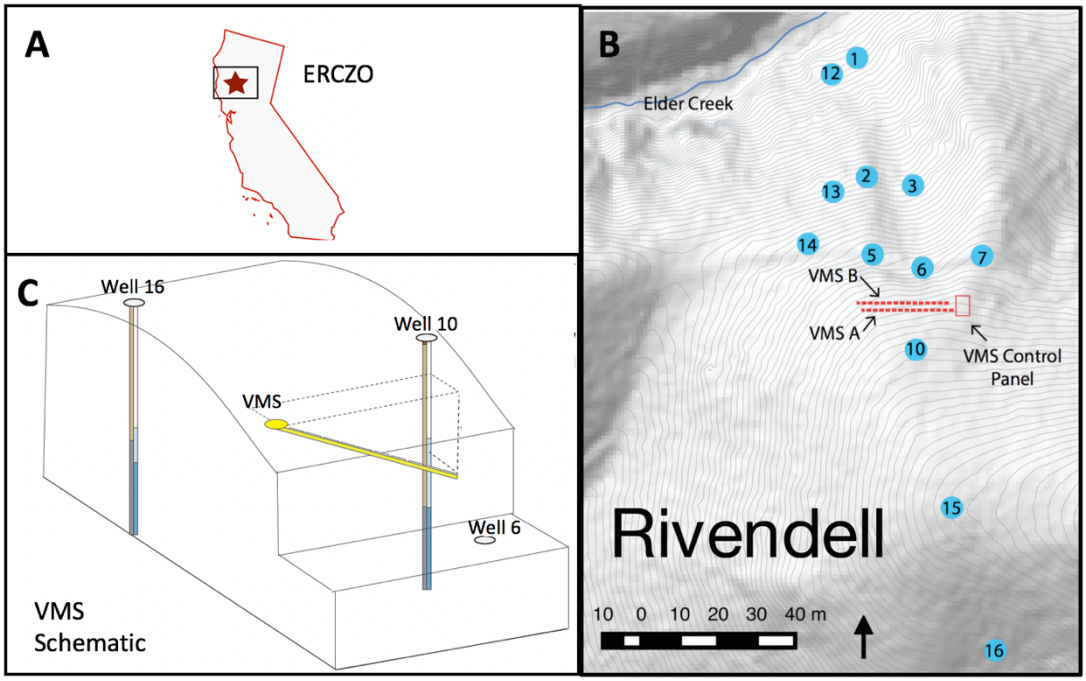

Figure 1. Panel A: Angelo Coast Range Reserve in northern California. Panel B shows an elevation contour map of the field site and location of vertical wellbores (blue circles) and the VMS indicated by the red dashed lines. Panel C: Orientation of VMS boreholes into the hillslope at approximately 55° (Druhan et al., 2017).

VMS – A, VMS – B, groundwater wells, and Elder Creek fluid samples are all collected on a bi-weekly interval. Once the fluid is extracted from a given depth, aliquots are filtered using a 0.22-micron filter and stored in 15ml vials for cation analysis. pH is measured in the field as soon as samples are extracted from below ground. pH measurements taken after August 2016 were conducted using an Accumet pH probe. Cation samples are acidified with approximately 0.05ml of double distilled concentrated nitric acid (HNO_3 at 15.8M) to a target pH of approximately 1.5. These samples are refrigerated and promptly transported to University of Illinois at Urbana-Champaign for laboratory analyses.

3.2 Fluid sample analysis

Cation samples are refrigerated at about 4 degrees Celsius prior to analysis using a Thermo Fisher Scientific iCAP-Q Inductively Coupled Plasma Mass Spectrometer (ICP-MS) for major, minor, and trace elements. The instrument uses a He collision cell (KED mode) to reduce polyatomic interferences. To prepare for analysis, samples are diluted with 2% HNO_3 in 4M hydrochloric acid-cleaned plastic tubes to ensure concentrations are within measurable range for ICP-MS. An internal standard consisting of rare elements (Sc, Ge, Y, Rh, In, Tb, Ho, and Bi) at 1 ppb is mixed into the sample stream on line to monitor and correct for instrument drift and matrix effects in the plasma. Additionally, bracketing reference standard ADM_TMIMQ1_70A (Waters ERA, eraqc.com) was analyzed every 10 samples to provide a secondary standard with a solute matrix closer to that of the samples. Minor corrections were made based on deviations of measured concentrations in bracketing standards from known values (Eq 1). Measurement precision, calculated from the standard deviation of the bracketing reference samples, was found to be 1.3% for Ca, Na, K, and Mg, and 4.7% for Si. The measured concentrations of major cations and Si for water samples are corrected based on the measured reference standard via the following equation:

$$[C] = \frac{[C_{ADM}]}{[C_{ADM,meas}]} \times [C_{unknown,meas}] \quad \text{Eq. 1}$$

where $[C_{ADM}]$ is the reference concentration, $[C_{ADM,meas}]$ is the measured concentration of the standard, $[C_{unknown,meas}]$ is the measured concentration of unknown samples, and C is the corrected concentration of unknown samples.

3.3 Batch reactor design

Three batch weathering experiments were conducted using shallow (~1.5 m), middle (~7.8 m) and deep (~16.4 m) solid material recovered from installation of the VMS. In each batch reactor, crushed regolith (4 – 5 g with average grain diameter <1.5cm) was place into a sealed double walled glass container filled with ultrapure (Milli-Q) water (pH = 5.9) with a small, closed headspace containing air at the top (Table 1). In all reactors the solid phase was completely submerged. A long needle and pH probe were used to sample fluid and monitor pH changes for the duration of the experiment (Figure 2). An acid-cleaned bar magnet was used to continuously stir the fluid and rock within the batch reactor on a low setting. Fluid samples extracted from the batch reactor were filtered using 0.22-micron filters, aliquoted and stored in two 4ml pre-cleaned plastic tubes. One aliquot of sample was acidified with HNO_3 and kept in a refrigerator until ICP-MS analyses. The other sample was filled to the top without acidification to minimize head-space and kept refrigerated for ion-chromatograph analysis. The mass of each sample extraction was recorded to calculate the final fluid volume of the container. We account for the potential effects associated with this small loss of fluid volume using our numerical simulations. All reaction network models are run using two starting solid:fluid ratios, one corresponding to the value at the beginning of the batch experiments, and one corresponding to the value at the end (Table 1). This allows us to bound the extent to which fluid concentration changes are influenced by the small decrease in fluid volume with every sampling.

Table 1. Batch reactor solids, initial water volume added, and final water volume remaining after last sample collection.

	Depth of crushed regolith (m)	**Mass of solids (g)**	**Initial volume of fluid (L)**	**Final volume of fluid (L)**
Shallow	1.5	4.8652	1.26	1.07
Middle	7.8	5.229	1.16	1.00
Deep	16.4	4.1960	1.20	1.10

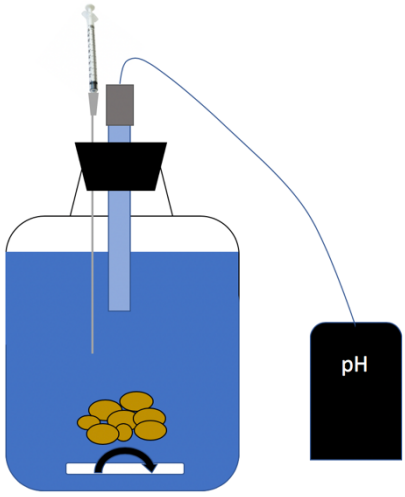

Figure 2. Diagram of batch reactor setup. A pH probe is installed within the batch reactor to continuously monitor the pH. A long sampling needle is used for fluid extraction throughout the experiment.

Our batch reactor experiments were performed as closed systems without buffers to constrain pH or regulation of the gas headspace in the vessel. This choice was made intentionally, as fluctuations in these parameters are considerable across the vadose zone of the ERCZO and do not justifiably support regulation in the reactors. Further, constraining the pH and pCO_2 of the reactors would influence the extent to which minerals equilibrate with the fluid. Instead, we elected to let the systems evolve from known initial conditions to final steady state solute and (small) headspace compositions and utilize a multi-component reaction network model to simulate this progression. Though these isolated systems are clearly distinct from the conditions of the ERCZO vadose zone, they are closer to the natural system behavior than a completely buffered reactor. In this way, we may develop a batch reactor-constrained reaction network model, and then implement this within a larger multicomponent reactive transport model to represent the appropriate boundary conditions of the field system. Thus, pH may be viewed as a variable which we track along with solute concentrations from the suite of observations we draw directly from the VMS.

3.4 Solid phases characterization

Parent bedrock underlying the ERCZO hillslope is characterized using an average of the of the deepest regolith collected from four vertically drilled wells, as well as bedrock exposed in Elder Creek (Figure 1B). Deep, Middle, and Shallow sample depths are represented by the

average mineral volume fractions recovered from corresponding samples recovered during the installation of Well 10 and Well 14 based on XRD analysis Gu et al., (in review). Pyrite concentrations were estimated from the weight fraction of sulfur from elemental analysis.

The specific surface area (SSA) of minerals are difficult to constrain due to the strong influence of grain size on available surface area and uncertainty in mineral surface accessibility (Beckingham et al., 2016; Heidari et al., 2017). Therefore, the specific surface areas for any given mineral may vary by several orders of magnitude. Given this uncertainty, we obtain an initial estimate of the mineral specific surface area by partitioning the SSA_{bulk_rock} according to mineral volume fractions. The specific surface area of each mineral used in batch reactor model is then calculated as

$$SSA_{mineral} = \frac{Volume\ Mineral}{Volume\ Rock} \times SSA_{bulk\_rock\_deep}\ [m^2 g^{-1}] \quad \text{Eq. 2}$$

where $SSA_{bulk\_rock\_deep}$ is estimated from neutron scattering of the deep rock sample (Gu et al., (in review).) These calculations are adjusted within a few orders of magnitude iteratively, in the modeling process, to better optimize the reproduction of the experimental data while fixing kinetic rate constants derived previously from other studies. The same mineral specific surface area for each mineral is used across all batch reactor depths (Table 2).

Table 2. Regolith composition and surface area at each depth interval

Mineral	**Initial mineral volume fraction**			**Specific surface area [m^2/ g rock]**	
	Shallow Depth (1.5m)	Middle Depth (7.8m)	Parent Bedrock (16.4m)	Batch reactor	1D/2D Model
quartz	0.29	0.25	0.26	3.80	3.80×10^{-2}
albite	0.14	0.21	0.23	3.40	3.40×10^{-4}
dolomite	BDL*	BDL*	0.02	0.0033	3.3×10^{-6}
chlorite	0.14	0.14	0.16	2.31	2.31×10^{-2}
kaolinite	0.10	0.09	0.04	0.55	5.46×10^{-3}
smectite	0.16	0.11	0.12	1.75	1.75×10^{-2}
fe(hydr)oxide	3.15×10^{-3}	4.93×10^{-3}	BDL***	0.07	7.2×10^{-2}
microcline	0.01	0.02	0.01	0.16	1.16×10^{-3}
muscovite	0.08	0.09	0.08	1.16	1.16×10^{-2}
illite	0.07	0.08	0.08	1.11	1.1×10^{-2}
pyrite**	4.0×10^{-5}	6.2×10^{-5}	9.8×10^{-4}	0.014	1.4×10^{-5}
organic carbon****	9.129×10^{-7}	5.026×10^{-7}	9.593×10^{-7}	0.013	1.3×10^{-3}

*Below detection limit of 0.5 w.t % for dolomite

**Pyrite estimation from elemental concentration of sulfur

Table 2 (cont)
***Below detection limit for fe(hydr)oxide
****Estimation of organic carbon in sedimentary rock comes from LECO combustion

3.5 Reaction network model for the batch reactor data

The three batch reactor experiments were simulated as 0D models (i.e., closed systems without transport) using the numerical reactive transport software CrunchTope (Steefel et al., 2015). To simulate these systems, the domain was fixed at a partial fluid saturation state equivalent to the volume of the batch reactors less the headspace. The initial fluid is equilibrated with atmospheric pCO_2 and pO_2 at the start of the simulation and both the liquid and gas phases evolve with reaction progression. The simulations are run for a duration of 150 hours. Kinetic rate constants (Table 3 below; references provided) used in these simulations are obtained from a compilation of parameters for geochemical modeling and were not adjusted in our model simulations. The use of these rate laws and literature parameters yielded robust simulations for most of our batch reactor fluid solute evolution series, however, modeled sodium and potassium concentrations were systematically lower than our observed values. This suggested an additional rate dependence which we introduced an additional rate law with pH dependence to increase the dissolution of albite and microcline at low pH. This approach is commonly employed to incorporate the strong dependency of mineral reaction rate due to variations in pH (e.g. Wen & Li, 2018). The observed pH varies from ~5 to ~8 in the fluid of the VMS and thus, we wish to express the overall reaction rate of primary silicates (i.e., albite and microcline) as the sum of both rate laws. The kinetic rate constants for these two pH-dependent rate laws were adjusted slightly in order to achieve better sodium and potassium results. As noted above, small adjustments to the specific surface area of each mineral were implemented in order to improve the simulations. Thermodynamic parameters at 25^{o} C were similarly constrained from studies compiled in Helgeson (1978) and Wolery et al. 2007.

Table 3. Kinetic rate and thermodynamic parameters for each mineral and reference

Mineral and chemical composition	**Kinetic Rate Log *k* [a] [mol m^{-2} s^{-1}]**	***Log k Reference***	***Equilibrium Log $K_{eq,25C}$*** [f]
quartz	-13.40	Tester et al., 1994	-4.0
dolomite	-7.53	Arvidson and Mackenzie, 1999	4.0
albite	-4.2[b] , -11.82	Chou & Wollast 1985	2.8
microcline	-4.2[c] , -12.41	Blue & Stillings 1995	-0.28
chlorite	-12.52	Nagy 1995	32
illite	-14.8	Kohler et al., 2003	9.0
smectite	-12.78	Bauer & Berger, 1998; Huertas et al., 2001(a)	17
muscovite	-13.00	Nagy 1995	14
kaolinite	-13.18	Carroll & Walther, 1990; Ganor et al., 1995	6.8
Fe(hydr) oxide	-14.00[d]	Run and Gilkes (1995)	3.0
pyrite	-4.55	McKibben & Barnes, 1986	22
organic carbon	-10[e]	--	

[a] Log k parameters obtained at neutral pH at ~25° C
[b] Parallel rate for albite with pH dependence
[c] Parallel rate for microcline with pH dependence
[d] Estimation of rate from hematite
[e] Chosen to regulate the rate at which organic carbon solid dissolves
[f] Thermodynamic parameters from Helgeson (1978) and Wolery (2007)

3.6 Constraining cation exchange capacity

These simulations also allow ion-exchange reactions on mineral surfaces. This allows the preferential exchange of cations onto surface exchanger sites that are governed by an ion-exchange coefficient analogous to that of thermodynamic equilibrium constants. In our model, we assign a cation exchange capacity which is the sum of the total charge equivalent concentrations of adsorbed cations. These values are obtained from previous experiments reported by Kim et al., 2014 for deep, middle, and shallow solids obtained from the ERCZO (Table 4). Ion coefficients are expressed using the Gaines-Thomas convention, where preference for ion attachment to surface site is normalized to the same ion (Appelo and Postma, 1993). For this study, the relationship between competing species for surface exchange sites is calculated relative to binary exchange

with sodium. These ion selectivity coefficients (K_{GT}) for the vadose zone at the ER-CZO are calculated from Kim et al. (2014) as 1.26×10^{-7}, 5.01×10^{-7}, and 5.89×10^{-3} for Ca, Mg, and K respectively.

Table 4. Cation exchange capacity and selectivity coefficient values from Kim et al., 2014 supplementary information.

Depth (m)	CEC* [eq g^{-1} solid]
Shallow (1.5)	1.43×10^{-3}
Middle (7.8)	2.27×10^{-3}
Deep (16.4)	1.58×10^{-3}

* Cation exchange capacity reported from Kim et al., 2014

3.7 Parameterization of regolith at ERCZO

A set of 1D models were constructed as an extension of the batch reactor simulations, where single mineral assemblages of shallow, middle, and deep depth interval of the VMS-B borehole were used for the whole model domain and dilute fluid is advected through at 3 m/yr (Fig. 3). Thus, in the present study, we approximate the annual flow rate using total measured precipitation less the average values lost due to a tree canopy interception (IT) and evapotranspiration (ET) in the following way:

$$v = \frac{Precipitation_{total} - ET - IT}{\varphi_{flow}} \quad \text{Eq. 3}$$

where φ_{flow} is the component of the porosity which is assumed to be connected and open to fluid flow. This flow rate is discussed in further detail below (section 5.8). We choose to use a domain porosity of 20% to account for both the pore space in the rock matrix (4-10%) as well as the increased exposure of connected space in the subsurface due to the penetration of fractures. The dilute, inflowing fluid in the 1D model is compositionally the same as that of the fluid in the initial condition of the batch reactor experiments. In each of these models, dilute fluid is advected through a single mineral assemblage 18 meters thick (where each cell length is 18 cm) until steady state concentrations are reached. We verified the initial condition of the system is erased by the depletion of an inert tracer with an initial concentration of 0.001M across the domain but subsequently flushed with infiltrating fluid from the inlet boundary condition. At 50 years of simulation, the concentration of the inert tracer is negligible across the entire domain. We observe sparingly small changes to the initial mineral volume fractions in these models over a short course

of 50 years of simulation (i.e. changes caused by weathering in from the initial solid composition profile). Thus, we are seeing the direct influence of the imposed solids on solute composition and not the alteration of the solid due to interactions with fluid over time.

A partial fluid saturation of 50% is used for all 1D numerical simulations to represent the unsaturated condition observed in the field. While this saturation fluctuates throughout the profile, the measurement of the exact water content is arguably less significant in the examination of our model at present. Instead, we choose to represent an average partial saturation throughout our domain to ensure an overall representation of the effects of reactive gasses within our simulations. We choose to capture this by choosing a balance between the partial saturation, allowing high volume of gas to diffuse into the domain, and the oxidation of organic carbon within the profile. Within the model framework, this value allows sufficient communication with the upper boundary condition to ensure that gas phases are able to diffuse freely. The corresponding fluid content equivalently allows sufficient volume for reactions to proceed without immediately saturating. Elevated pCO_2 is observed in the VMS, deep in the subsurface (Tune et al. in prep). The source of this high pCO_2 is beyond the scope of the present study, but is likely due to the oxidation of organic carbon via microbial respiration and from tree root exudates. In the batch reactor experiments, we assume that such a source of labile organic carbon from biological activity and trees is not available as a driver of water-rock reactivity. However, based on the observations provided by the VMS (Tune et al. in prep) these effects cannot be ignored in the 1D and 2D reactive transport models if we are to accurately characterize reactivity across the vadose zone at the field site.

In order to account for this production of $CO_2(aq)$ within the domain and its associated reactivity, we include an artificial organic carbon solid which readily dissolves and acts as a proxy for rapid delivery of labile carbon sources. The high pCO_2 observed deep in the vadose zone is then linked to the oxidation of this labile carbon as a result of the availability of high pO2 content observed in the VMS. Accounting for this oxidation pathway directly, rather than simply fixing a high pCO_2 at depth, is crucial to the distribution and availability of $O_2(aq)$ for the oxidation pyrite, which is present in low volume fractions in the domain but is extremely reactive. In order to reasonably simulate the pCO_2 observed in the VMS, we have added 2% organic carbon solid at a depth range of 7.25-9 meters to simulate the increase of CO_2 observed in the gas profiles. The solid organic carbon is a negligible 0.002% everywhere else in the domain. The fluid is equilibrated to atmospheric $O_2(g)$ at the inlet and advected through the rest of the profile. A gas diffusion

coefficient of 0.01 cm^2/s is fixed in the model to allow for the high gas exchange into the system due to the presence of a well-connected fracture network.

Additional adjustments were made between the laboratory closed-system batch reactor experiment and field site to account for the change in available surface area between laboratory experiments and field observations. This surface area adjustment is commonly necessary in reactive transport studies where application of laboratory measurements of specific surface area are decreased by several orders of magnitude in order to simulate a robust comparison to field observations (Navarre-Sitchler & Brantley, 2007; Swoboda-Colberg & Drever, 1993; Velbel, 1993; A. F. White & Buss, 2013).

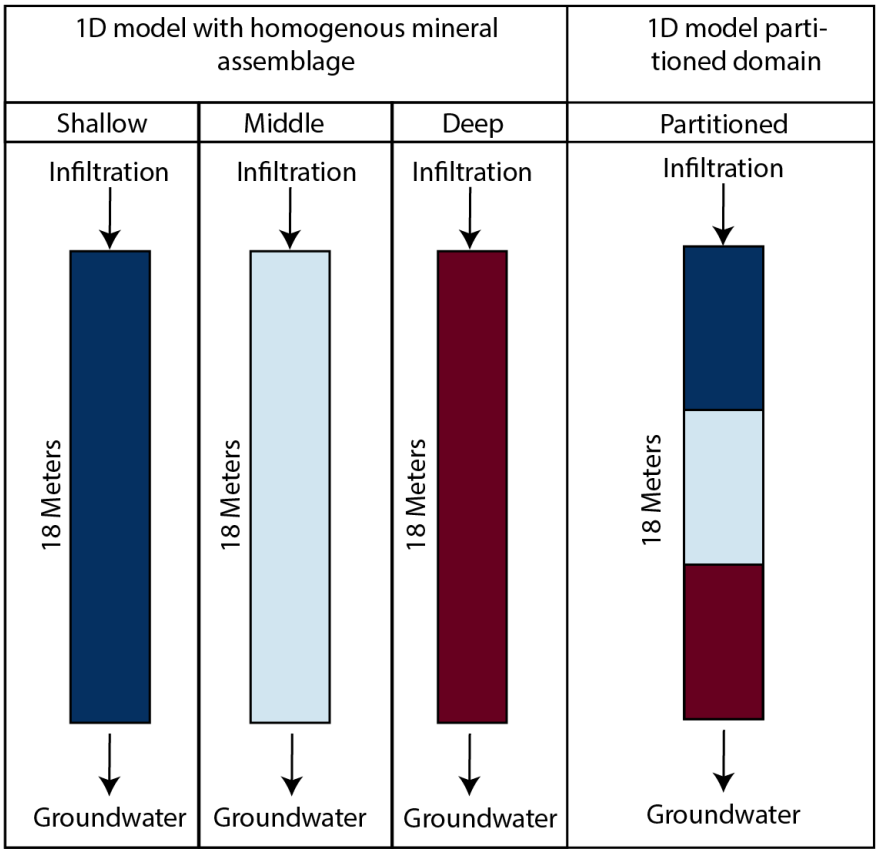

Figure 3. Conceptual framework for four 1D models. Each model domain is demonstrated by different color. The shallow, middle, and deep depth mineral assemblage is represented by dark blue, light blue, and dark red respectively. The partitioned model domain is sequentially assembled in the order of shallow, middle, and deep from the surface to the bottom. Fluid enters the regolith at the surface and exits at the bottom, spanning the range from infiltration to groundwater.

3.8 Parameterization of 2D model

The 1D model is inherently a simplification of what is a structurally complex bedrock system. As described above, the regolith of this region is primarily composed of a highly fractured argillite. To explore the general implications of a fracture-matrix system, we implement a 2D domain in our reactive transport model to include a fracture which sits adjacent to a matrix block as a means of constraining the extent to which the simplification of a 1D porous media influences the concentrations observed in the model. We impose a ratio of fracture aperture to domain width of approximately 0.15 (Figure 4), a higher ratio than observed in most natural shale bedrock (Gale et al., 2017; Ortega et al., 2006) but potentially achievable in such a highly weathered regolith. Thus, we would anticipate that in a domain more appropriate to coherent shale bedrock, the size of the fracture relative to the size of this matrix block would be even smaller, bringing the domain closer to that of a matrix domain. Thus, while the fluid flow rate may be orders of magnitude higher in the fracture, the effective volume contribution to the whole system is small. Thus, we would at expect lower fracture to matrix space ratio would produce an even less distinct solute concentration from the 1D model. In this sense we are creating as distinct of a scenario as possible from our prior model. To implement the fracture into the domain, we increased the porosity from 0.2 to 0.5 in the fracture and adjusted the mineral volume fractions accordingly. We maintained a uniform saturation of 0.5 which allows for the diffusion of gases across the domain, but the higher porosity of the fracture inherently allows more gas into this subsection.

The permeability of the fracture ($k_f = 1 \times 10^{-9}\ m^2$) is one order of magnitude higher than the matrix block ($k_m = 1 \times 10^{-10}\ m^2$) to simulate the inherently higher connectivity of this subdomain. The left and right boundaries are closed to prevent any fluid from exiting laterally. A vertical flow from top to bottom is induced by a fixed pressure gradient which is evenly imposed between the top and bottom boundaries. Due to the differences in permeability and porosity of the fracture and matrix subdomains, the flow velocity varies by approximately an order of magnitude between them. Thus, the magnitude of the pressure gradient is set such that the average flow velocity ($\bar{v}$) across the bottom boundary is 3 m/yr, comparable to the 1D flow model

$$\bar{v} = \frac{\sum_{i=1}^{i=n} v_i A_i}{\sum_{i=1}^{i=n} A_i} \quad \text{Eq. 4}$$

where v_i is the downward flow velocity in an individual cell (i) in the row spanning from cell 1 to cell n comprising a given depth, A_i is the cross-sectional area of each cell water is draining across at a given depth in this row, and $\bar{v}$ is the resulting average velocity of the cross-section. This approach allows us to compare solute concentrations between the 1D model and a flux weighted average value for the 2D model at any given depth. We generate these flux-weighted average values of solute concentration ($\bar{c}$) at depths across the 18-meter profile for comparison to the 1D model. The concentration is weighted by the flux of fluid through each cell as:

$$\bar{c} = \frac{\sum_{i=1}^{i=n} v_i c_i A_i}{\sum_{i=1}^{i=n} v_i A_i} \qquad \text{Eq. 5}$$

where c_i is the concentration of the solute in each cell (i).

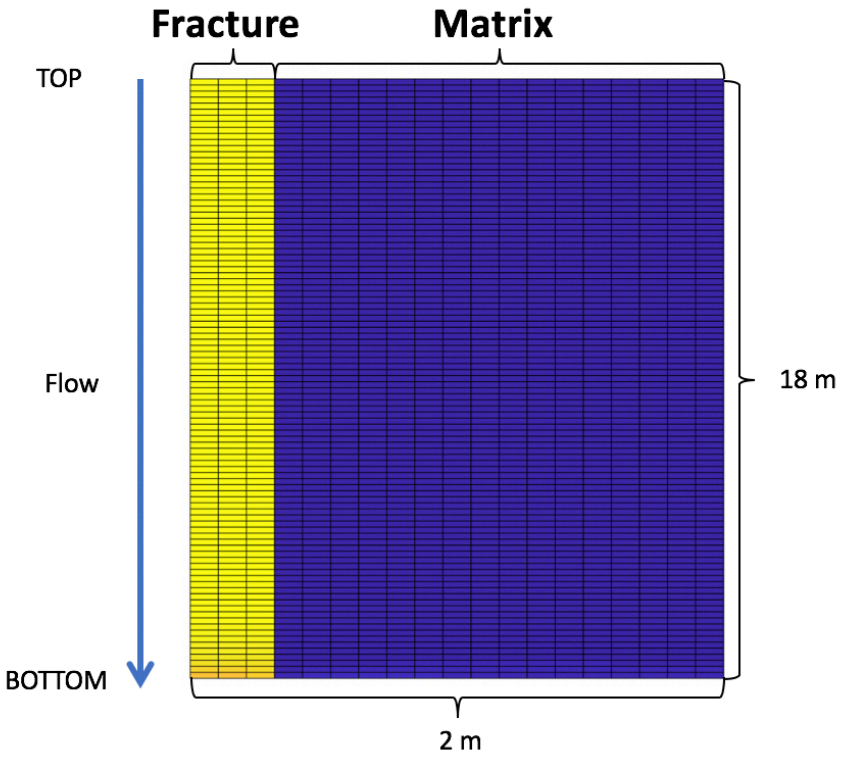

Figure 4. The conceptual diagram of our 2D model with a single fracture (yellow cells) adjacent to a matrix block (blue cells).

CHAPTER 4: RESULTS

4.1 Fluid geochemistry characteristics in the vertical structure of the vadose zone

The complete dataset of solute concentrations obtained from the VMS reflects a variety of water-rock interactions and transport pathways. In all samples, solute composition is influenced by the vertical drainage of water through the partially saturated vadose zone at this location on the hillslope. However, periodic elevation of the water table, notably during the later months of the wet season, often results in complete saturation of some of the deeper ports. Under these conditions, the solute composition is also a result of the lateral drainage of groundwater from up gradient to the location of the VMS. To isolate the effects of vertical heterogeneity on solute concentrations, we thus begin our analysis by omitting samples containing fluid contribution from lateral flow. These samples are identified by extrapolation of groundwater table heights from two adjacent wells (Well 7 and Well 10), correction for elevation differences and correlated to the elevations of VMS-A and VMS-B samplers. Those ports identified as below the water level of both extrapolations from W7 and W10 at the time of sampling were removed.

Partially saturated sample concentrations are illustrated (Figure 5A-5E) for major cations taken from the VMS-A. Here, we observe both the concentration, and the variability increase of Na and K as a function of depth. For example, sodium concentrations generally increase from an average of 0.19 ± 0.03 mM at 2m to 0.90 ± 0.60 mM at approximately 17 meters depth (Fig. 5A). The higher variability of Na at depth coincides with seasonal changes, where concentrations are generally lower during the dry period (May-September) and higher during the wet period (October -April). In contrast the variation in some solute concentrations remains low across the depth profile, despite a clear increase in mean value. For example, magnesium shows an average of 0.1 ± 0.06 mM until 8 meters depth, before increasing to a mean of 0.47 ± 0.03 mM by 17 meters (Fig. 5B). Potassium concentration profiles show little variation along the depth profile until 10 meters and then increase slightly by 17 meters (Fig. 5C). In contrast, mean calcium concentrations in VMS-A remain ~0.2 to 0.4mM until approximately 7m and then increase to 1.86 ± 0.14 mM with further depth (Fig. 5D). Silicon displays a unique trend compared to other major cations, in which concentrations increase initially and then decrease after reaching a maximum inflection point roughly 8 – 10 meters below ground surface (Fig. 5E).

Major concentration vs. depth profiles for the passive sampling system (VMS-B) largely follow those illustrated for VMS-A (Figure 6A-6E), where concentrations increase with depth

from the surface to the water table. A clear example is given by sodium (Fig. 6A), which generally increases from an average value of (0.2 ± 0.04 mM) at 2 meters to (0.6 ± 0.06 mM) at 16 meters depth. Mg concentrations (Fig. 6B) remain low (~0.07 ± 0.03 mM) in the shallow depth profile (1.5-6 meters) before generally increasing to 0.77 ± 0.04 mM across the interval from 6 to 16 meters depth. In contrast, potassium and calcium (Fig. 6C and 6D) show some initial decrease with depth, reaching minimum concentrations, before increasing with further depth below what is presumably the interval of active rhizosphere-driven nutrient cycling. The mean Si concentration is similar to the profile in VMS-A, increasing initially and then subsequently decreasing after reaching a maximum at roughly 10 – 12 meters below the ground surface.

Notably, across the wet (3,354 mm precipitation received from October 1, 2016 to May 31, 2017) and dry (32 mm precipitation received from June 1, 2017 to September 30, 2017) periods of the year, sodium concentrations at a given depth interval show comparatively weak correlation to the volume of precipitation received through the vadose zone (Fig. 6A) and there is almost no effect at all on Si concentrations (Fig. 6E). For example, at a depth of approximately 11 meters in VMS-B, Na and Si concentrations vary about their mean values by 0.41 ± 0.09 mM and 0.47 ± 0.06 mM respectively. In contrast, the average Na and Si concentrations increase by an average of 0.27 mM and 0.30 mM respectively over the depth interval from 3 m to 11 m below land surface. A similar pattern is observed in the Na profile of VMS-A, where the variation about the mean concentration at approximately 11 meters is 0.60 ± 0.23 mM, while the concentration increases by an average of 0.36 mM over the depth interval from 3 to 11m below land surface. In total, this observation suggests that the variability in these ion concentrations occurs as a function of depth through the vadose zone, rather than as a function of season (or associated fluid residence time) at a given depth.

In contrast, Mg, K, and Ca average concentrations show a greater range of variation over time at a given depth, rather than as a change of the mean solute concentrations across the depth interval. For Mg, K, and Ca, variation about their mean concentrations at approximately 11 meters depth in VMS-B are 0.18 ± 0.13 mM, 0.02± 0.009 mM and 0.30 ± 0.24 mM respectively. The corresponding increases in mean concentration from 3m to 11m are 0.12 mM (237%), 0.002 mM (14%) and 0.23 mM (367%), respectively. A similar pattern is observed in VMS-A in these three ions, where variation about the mean concentration for Mg, K, and Ca is 0.31 ± 0.19 mM, 0.07 ±

0.05 mM and 0.64 ± 0.50 mM respectively, while the concentrations increases 0.22 mM (252%), 0.02 mM (27%) and 0.36 mM (147%) over the depth interval from 3 to 11m below land surface.

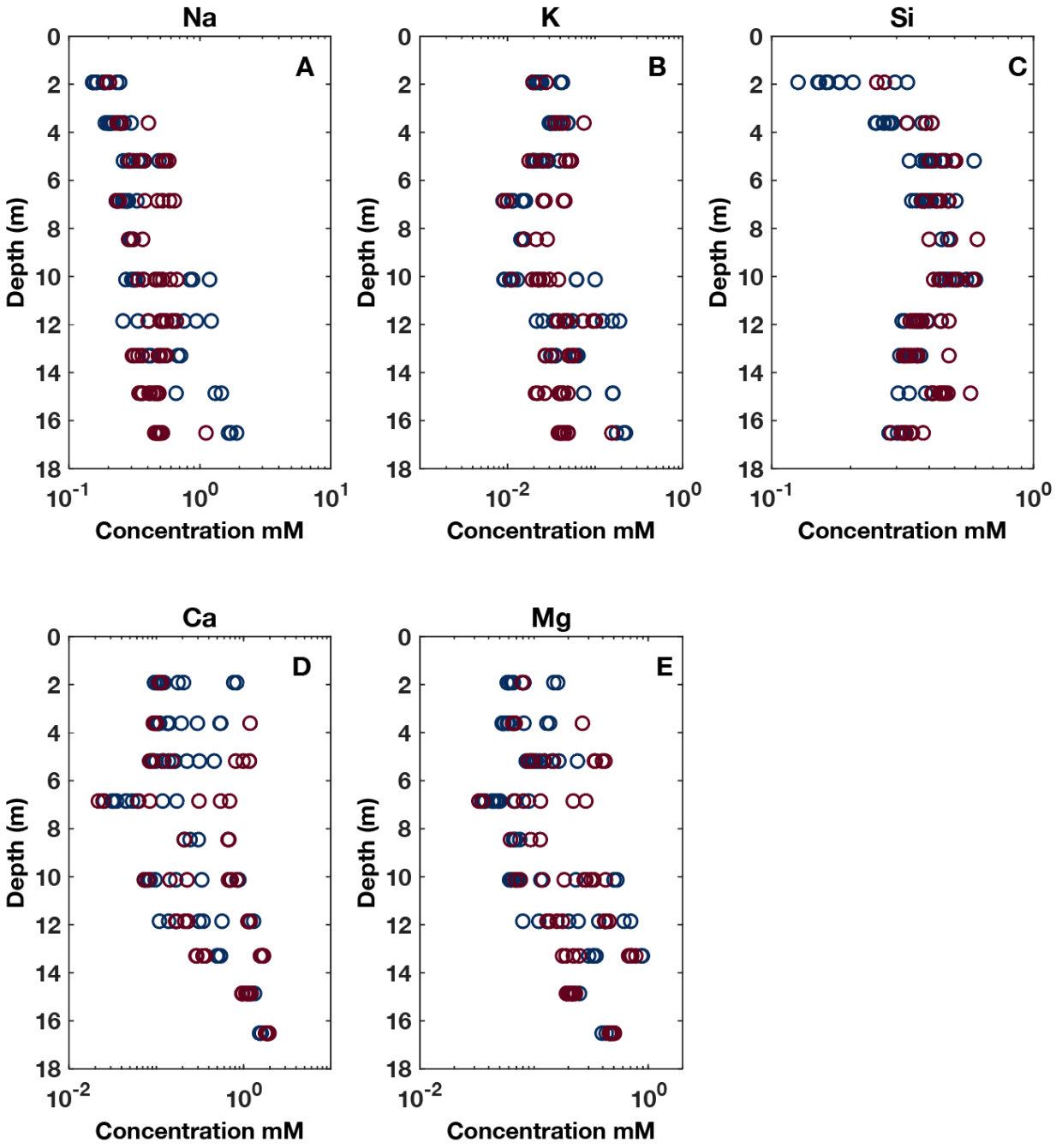

Figure 5. Na (A), Mg (B), K (C), Ca (D), and Si concentrations in fluid extracted from VMS-A ports across the profile of the vadose zone. The depth on the y-axis is corrected with the angle into the ground to display data as vertical distant below ground. Each point represents a single time point, with red circles denoting dry season (June – September) and blue colored circles denoting wet season (October – May). Samples were collected from July 2016 – December 2017.

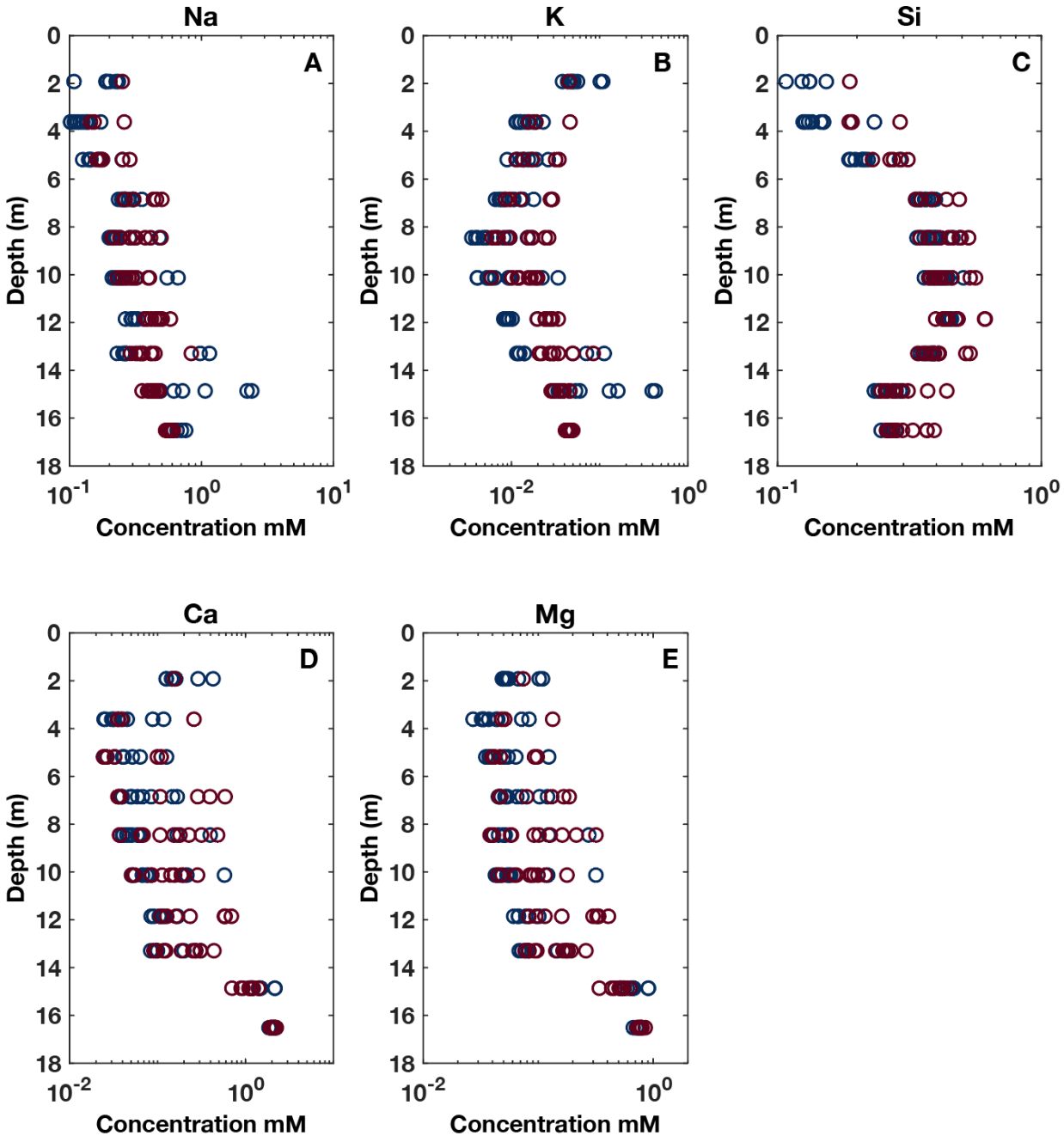

Figure 6. Na (A), Mg (B), K (C), Ca (D), and I(E) concentrations in fluid extracted from VMS-B (bottom row) ports across the profile of the vadose zone. Each point represents a single time point, with red circles denoting dry season (June – September) and blue colored circles denoting wet season (October – May). Samples were collected from July 2016 – December 2017.

4.2 Batch Reactor Experimental Results

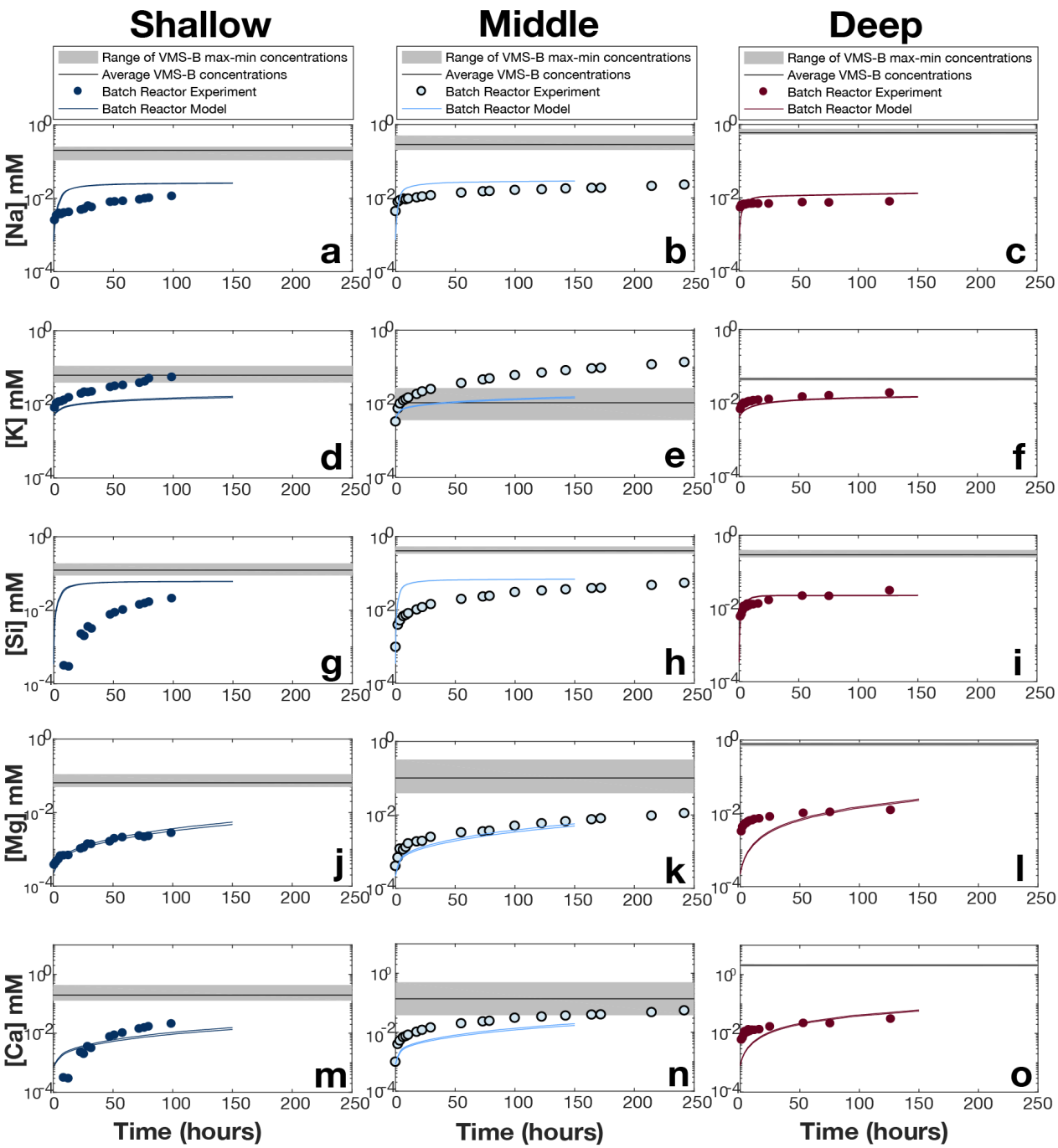

Figure 7. The grey shading outlines the range and black horizontal line marks the average concentration observed in VMS-B at the corresponding depth. Dark blue, light blue, and dark red points denote concentration time series of corresponding elements from batch reactor experiments and corresponding lines illustrate the reaction network model.

The batch reactor experiments were run for approximately 100-200 hours with fluid samples taken at set time intervals–of 2 - 4 hours in the first two days and approximately every 12

hours after. Concentrations for the shallow, middle, and deep samples all generally exhibit a rapid increase in major cation concentrations initially, which slows as time progresses and the reaction rates decreased greatly. While the decrease in reaction rates hints might suggest that the system is approaching some steady state, we cannot demonstrate the validity of such an inference over the limited time span of the experiments. In general, the time needed to reach steady state concentrations for elements Na, K, Si, Mg, and Ca (Fig. 7a-o) decreases with the depth at which the rock sample was recovered. For example, Si and Ca concentrations of the shallow depth experiments continue to rise rapidly over the first ~60 hours before approaching steady state (Fig. 7g and Fig 7m). In contrast, Si and Ca concentrations of the deep depth sample (Fig. 7i and Fig 7o) began to approach steady state at approximately 8 and 3 hours into the experiment, respectively. Other elements, including Na, Mg, and K, exhibit similar behavior, though with less rapid increase initially relative to Ca and Si.

We note that in the batch reactor concentrations above, we describe the system as approaching 'steady state', meaning the increase in concentration has slowed considerably approximately 100 hours into the experiment. We use this term rather than a true 'equilibrium', recognizing that over this span of time the system may approach an equivalence point where formation of secondary minerals may be sufficient to offset associated dissolution of primaries, thus controlling the concentration of observed major cations in the aqueous phase. This ambiguity in the batch reactor experiments is further addressed using our multi-component numerical model, where secondary minerals precipitation can be simulated based on given parameters of the physical experiment (e.g mineral assemblage, dissolution rates, saturation state). We note that some models resemble the corresponding experimental data more closely than others. For example, the experimental concentration vs. time series for Mg and Ca are nicely reproduced in both the rise of concentrations initially and the eventual plateau at about 100 hours. On the other hand, we observe model overestimation of Si and underestimation of K in the shallow and middle depths in both the initial rise as well as the eventual plateau. This difference may be due to discrepancies between the specific surface area of minerals in proportion to their volume fraction. However, despite these minor disparities, the simulations are reproducing trends with relatively close resemblance to the experimental data for a majority of cations.

Notably, concentrations established in the batch reactors are generally lower than the average concentrations of fluids recovered directly from VMS-B, the borehole from which the

solid phase was recovered. The evolution and extent of water-rock interactions is expected to differ between closed and open systems due to the differences in temperature and supply of reactants. In open systems, CO_2(aq) and O_2(aq) are governed by diffusive exchange between the atmospheric boundary condition and partially saturated porosity as well as fluid advected through the solid. In these batch reactor experiments, the initial concentration of CO_2 and O_2 are fixed from the initial small headspace in the sealed container. As reactions progress in the experiment, the CO_2 and O_2 are steadily depleted due to the inability to exchange openly with the atmosphere. Thus, batch reactor steady state concentrations are expected to reach steady state over a much shorter timescale as the reactive potential of the system is limited relative to the continuous open system.

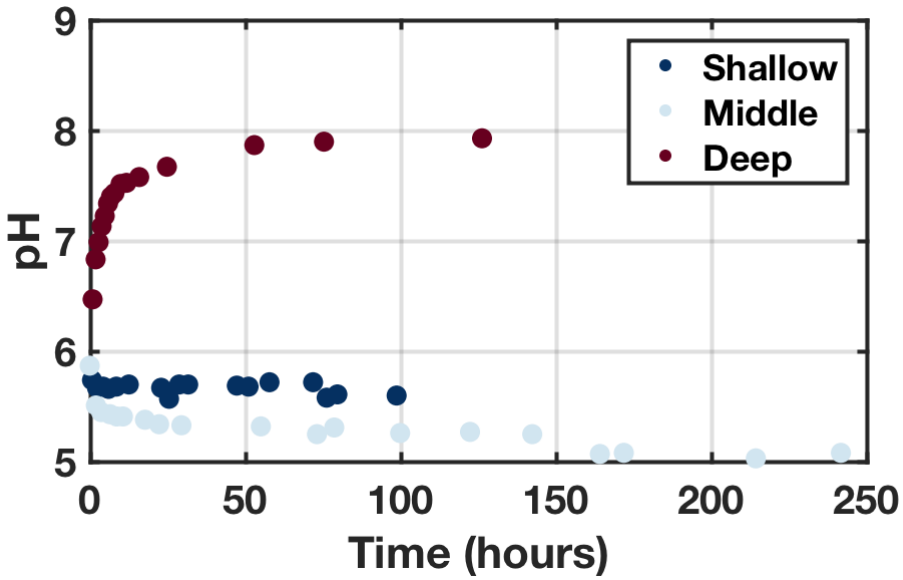

Figure 8. pH vs time series for batch reactor experiments.

The evolution of pH through time in both the shallow and middle depth batch reactors show that the pH reached steady state after approximately 3 hours with a slight decrease (~0.4 units and ~0.3 units respectively) from the initial condition (initial pH = 5.9) of the dilute fluid (Fig. 8). While the deep solid sample similarly approached a plateau over the duration of approximately 3 hours, the pH increases by approximately 1.5 units. Clear differences in the concentration of major cations, the length of time to reach steady state conditions, and the pH across the three experiments suggests that fluid interaction with each distinct set of mineral assemblage sequentially over the complete depth profile will impart a unique signature in comparison to discrete batch reactor experiments.

4.3 Batch reactor simulations in CrunchTope

In order to accurately simulate the evolution of concentrations in the open natural system, we use the CrunchTope reactive transport software to first simulate the simple, well-constrained batch reactor experiments and subsequently apply this calibrated reaction network to the 1D VMS profile. To constrain the reaction network for the batch reactor models, we created a closed 0D simulation using measured mineral assemblages and water:rock ratios for the three distinct depths (Table 1), and chemical reaction rates and thermodynamic equilibrium constants compiled from literature values (Table 3). Our batch reactor simulations (Figure 7) are implemented in a multicomponent reaction network representative of the time evolution and steady state concentrations obtained from our experiments. Initial conditions are the same across the batch reactor models with differences in varying mineral volume fractions, cation exchange capacity, and partial saturation as described above.

The concentrations of Na (Fig. 7a-c), K (Fig. 7d-f), and Si (Fig. 7g-i) are largely controlled by the dissolution of albite and microcline. We used pH dependent rate laws for both albite and microcline to facilitate additional dissolution at lower pH. These simulations show the concentration of Mg (Fig. 7j-l) and Ca (Fig. 7m-o), are controlled by the dissolution of carbonates, which are readily dissolvable by weakly acidic fluid. The parallel increase in both Mg and Ca concentrations in the batch reactor solutions suggests that the carbonate mineral in these samples is closer to dolomitic composition than a pure calcite endmember. Therefore, we represent carbonates in the system with dolomite and its associated kinetic parameters to facilitate mineral dissolution of both Mg and Ca. We assumed for shallow and middle depth models, there exists a small volume fraction of dolomite (0.5 w.t.%; below detection in XRD analyses) based on the observation of Ca and Mg concentration increase in the fluid.

We have previously described the system as approaching concentration plateaus, which are possibly influenced by secondary mineral precipitation occurring during the experiments. Accordingly, we have constrained the minerals likely to dissolve (calcite, albite, microcline, and pyrite) in this field site to dissolution only, whereas clays and other secondary phases included in the model are simulated using a reversible transition state theory (TST) rate law, such that they are able to precipitate. This approach yields an accurate approximation of the experimental data (Fig. 7) with only the adjustment of the specific surface area of minerals and the porosity. Notably, all other parameters remained unadjusted from our batch models and associated literature values. The

general similarity between the models and the experimental data is therefore quite good given the lack of tuning.

CHAPTER 5: DISCUSSION

5.1 Ion ratios

In total, our data suggest that some solute concentrations are principally regulated by depth, while others also vary to a similar extent from wet and dry seasons. However, these inferences are somewhat limited to the observation of differences across the vertical profile from shallow to deep. We thus further pursue this relationship between vertical structure and fluctuation in solute concentration over season and precipitation cycle by normalizing the cations to one another as a means of removing any effects of dilution, evaporation and (at least congruent) vegetation cycling across the depth profile (Figure 9A) for comparison. These ion ratios vary systematically with depth into the vertical profile. In general, [Ca]/ [Na] and [Mg]/[Na] decrease from the shallow ports to the middle ports and subsequently increase from the middle ports to the deeper ports for both VMS – A and VMS – B. Solute fluxes from silicate and carbonate-dominated catchments are shown from Gaillardet et al., (1999). Notably, Gaillardet et al. compiled these ion ratios for the 60 largest rivers across the world, demonstrating that dissolved ion ratios reflect the lithological signature from fluid-rock interactions. The [Ca]/[Na] and [Mg]/[Na] ratios from these rivers span a large range across evaporite, carbonate, and silicate dominated catchments. For example, a fluid sample from a river in a carbonate dominated landscape is generally high in Ca and Mg, resulting in elevated [Ca]/[Na] and [Mg]/[Na] ratios. Here, we observe that the ion ratios obtained from the VMS group near the Gaillardet silicate endmember for shallow and middle ports and trend towards the carbonate endmember in the deeper ports. This suggests that the fluid-rock interactions within our vadose zone profile reflect lithological changes, in which the shallow and middle depths are primarily dominated by silicate weathering until the carbonate weathering front is crossed in the deeper depths. This inference is supported by the solid phase mineral assemblage, where we observe a corresponding increase in the CaO w.t % in VMS-B from ~0.5% at near surface to 1.5% at approximately 17 meters. A corresponding increase of calcite weight percentage in the vertical profile of W10 is found to be up to 3% at 20 meters below the surface. This correlation suggests that the increase of Ca and Mg relative to other ions in the aqueous phase is due to the dissolution of carbonate in the deeper subsurface.

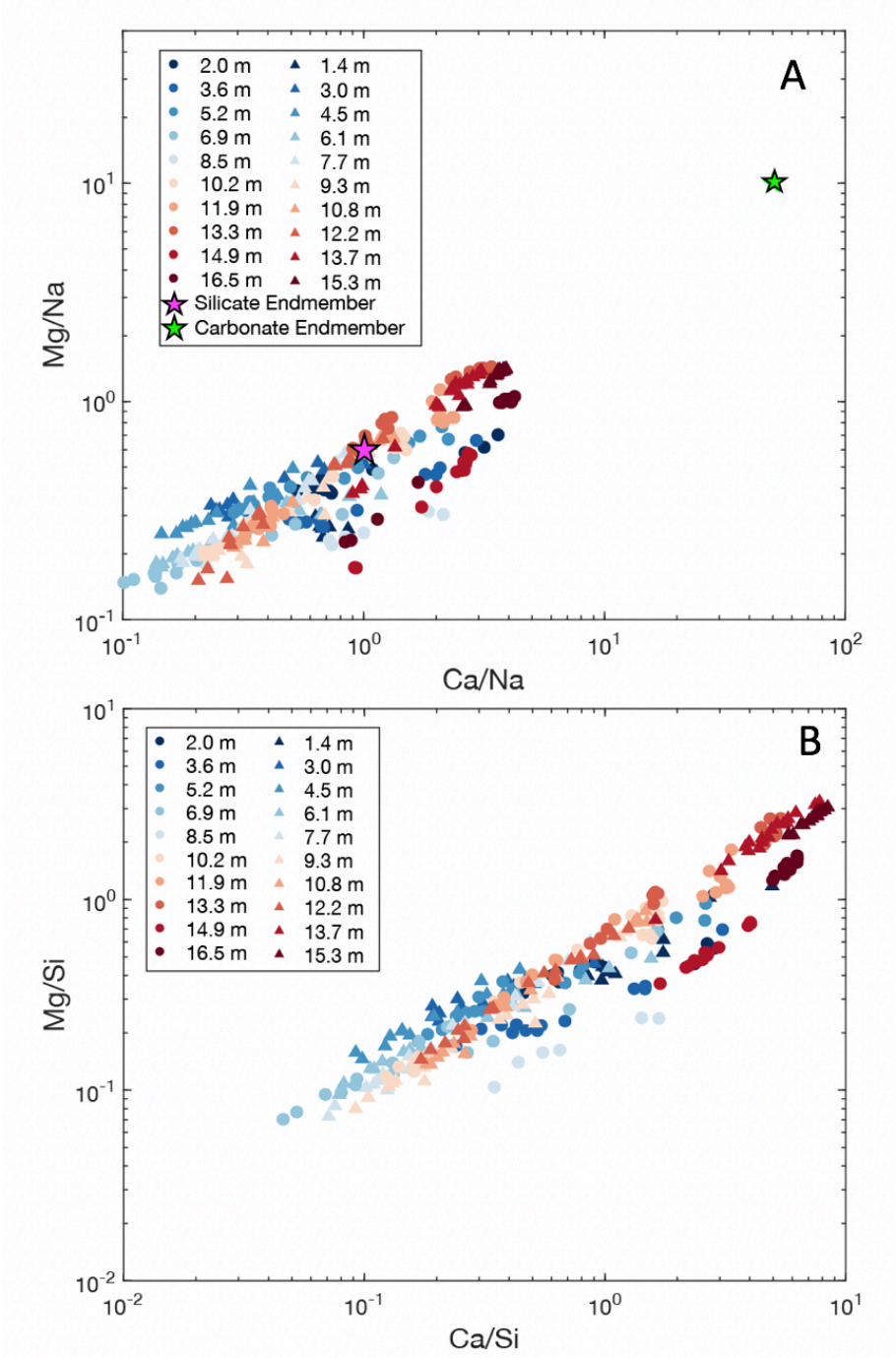

Figure 9. Ion ratio plot of [Mg]/[Na] vs. [Ca]/[Na] and of [Mg]/[Si] vs. [Ca]/[Si] in panel A and B respectively. Data are displayed from a systematic sampling campaign spanning the interval of July 2016 to December of 2017. The ion ratios are colored by depth into the subsurface, where dark blue points are close to surface and red points are deeper into the depth profile. Filled circles and triangles denote ratios from fluid samples extracted from VMS-A and VMS-B respectively. Ca and Mg concentration normalized to Na from primarily silicate and carbonate dominated lithology are denoted by magenta and green star respectively (Gaillardet et al., 1999).

In comparison to the batch reactor experiments, both the magnitude and trends of the corresponding fluid ion ratios from the VMS are very similar, suggesting that the chemical reactions occurring in the open structure of the natural system are recreated in the laboratory (Figure 10). Ca/Na and Mg/Na ratios of the batch reactors match the trend in ratios from VMS-A and VMS-B fluids across the vertical profile, though to a minor extent there are systematic offsets

between the two. The batch reactors for the deep regolith are generally slightly lower in [Mg]/[Na] ratios and similar in [Ca]/[Na] ratios to fluid recovered from VMS-B at the same depth interval. The middle samples show slightly higher [Mg]/[Na] ratios from the batch reactor fluid than that of VMS-B fluid. In contrast, the shallow depth [Mg]/[Na] and [Ca]/[Na] ratios are both generally slightly lower in the batch reactor than the fluid from VMS-B at the same depth interval. These small systematic offsets are likely associated with the effect of sequential transport of fluid from the shallow to the deep solid compositions in the natural system, where such subtle differences are undetectable in direct concentration vs. depth over seasonal periods.

A comparable pattern is also noted when we normalize to silicon concentrations [Ca]/[Si] vs [Mg]/[Si] (Figure 10B). Ratios from comparable depths between the batch reactor experiment and the VMS fluid values again cluster near each other but are slightly systematically offset. In general, the shallow batch reactor ratios are slightly lower in Mg/Si and Ca/Si than that of the corresponding VMS fluid. The batch reactor ratios of the middle depth are generally slightly higher in Mg/Si and similar Ca/Si ratios as corresponding depth of VMS fluid. In contrast, the deep depth generally shows slightly lower Mg/Si and Ca/Si ratios. The increase of Ca/Si ratios further supports carbonate dissolution in the deeper subsurface. Also, notably, normalization of ion concentrations to Si has been used to infer secondary clay precipitation, where depletion of Si relative to other ion concentrations (e.g. K, Ca) is an indicator Si partition into clays (Georg et al., 2006; Georg et al., 2007; Strandmann et al., 2014). The increase of Ca/Si ratios in the deeper depths of the VMS may be a result of such Si partitioning into clay phases. However, this is difficult to verify since the VMS crosses the carbonate weathering front at these deeper depths, resulting in an increase of [Ca] from the dissolution of this $Ca_xMg_{(1-x)}CO_3$ phase. Thus, the increasing [Ca]/[Si] ratio may be a combined signal of both carbonate dissolution and secondary clay precipitation. Further analysis is necessary to distinguish between such clay precipitation and carbonate dissolution signals using processes such as the mass-dependent fractionation of Li isotopes to confirm regions of active clay precipitation within the vadose zone.

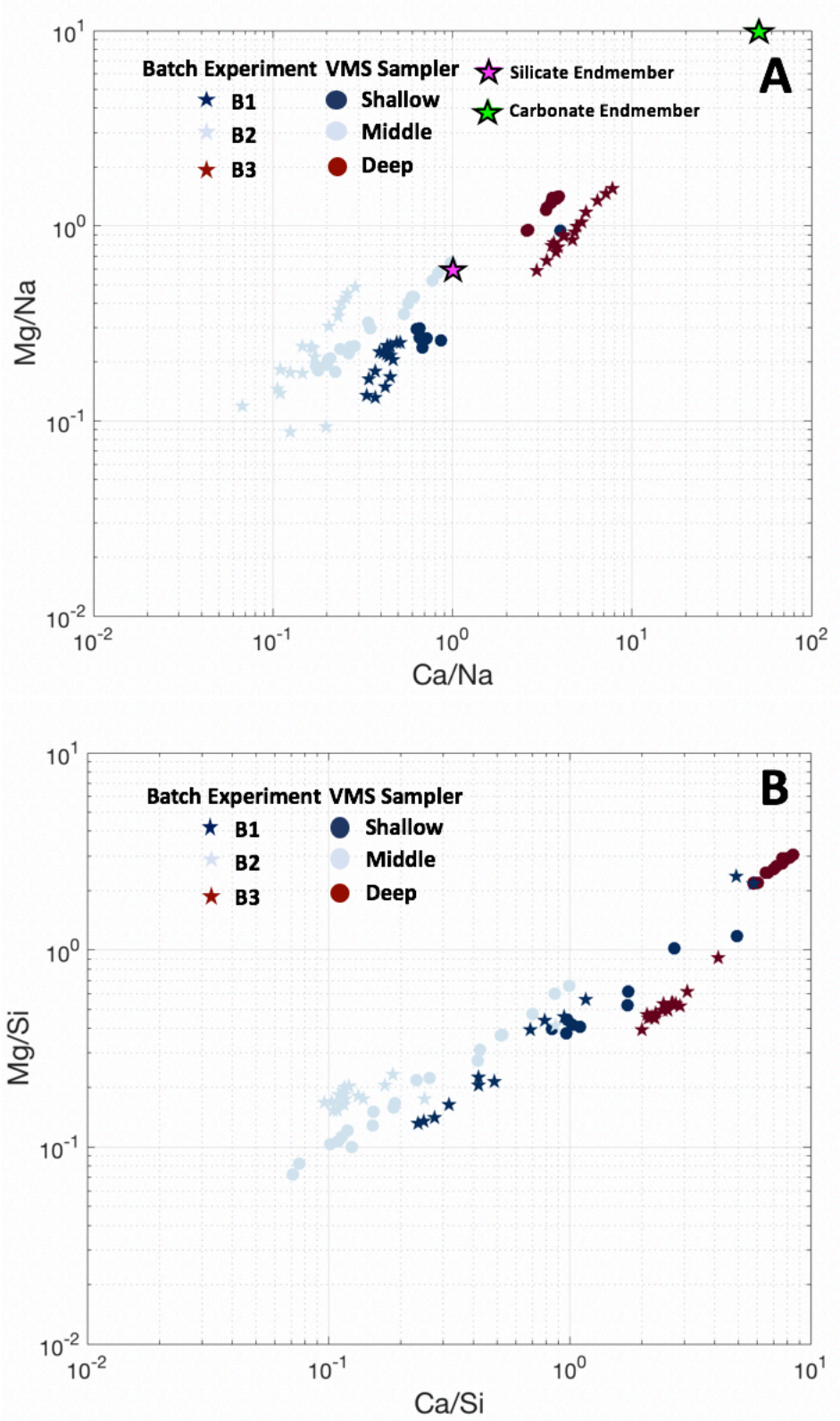

Figure 10. Comparing ion ratios of Ca and Mg normalized to Na and Ca and Mg normalized to Si in panel A and B respectively. Colored triangles denote observations from VMS-B and stars denote observations from batch reactors over the complete time series of each experiment at respective depths.

5.2 Batch reactor ion ratios across timescales

Above, we observe a clear spatial pattern in ion ratios of the vertical profile, and we show that spatial differences in solid composition are one driver of this pattern. However, these values also reflect the temporal scale over which these fluids are evolving, since concentration signatures are influenced by both the length of time the fluid interacts with the regolith and the type of minerals available. To disentangle these signatures, we turn to the batch reactors to isolate the concentration time series for each stage of weathering (shallow, middle and deep). Again, we make use of the ion ratios to isolate evolution in solute signature from influences of dilution and evaporation (Fig. 11). This technique is employed, as in previous studies, to quantify the influence of lithologic changes on solute signature in drainage networks (Gaillardet et al., 1999; Pogge von Strandmann et al., 2008, 2014). Thus, we expect the changes in ion ratios to reflect the lithologic gradient across the vertical profile of the regolith as the result of weathering.

Simulated ion ratios taken after the first 150 hours of the batch reactor experiments cluster closely near the range seen in the VMS fluid ratios, with clear distinction between spatial distribution of the shallow, middle and deep depths, suggesting that the fluid systematically evolves across the depth profile (Fig. 11A). Despite the drastically different time scale of fluid-rock interaction between the batch reactors and the appropriate time for fluid transport across the intact vadose zone profile of the ERCZO, these ion ratios show a clear evolution of increasing Ca/Na vs Mg/Na values from the shallow and middle depths to the deeper profile (Figure 11).

Assuming that fluid flows at approximately 3 m/yr across the vadose zone (discussed and tested further in section 5.9), and dividing the 18-meter profile into 10 cm sections, the fluid spends about 526 hours (22 days) in the top 0.18 meters of regolith. Thus, the batch reactor experiment results represent fluid ratios sampled at much shorter than the length of time we would expect fluid to spend interacting with minerals within the vadose zone. The numerical simulation then allows us to gain insight into the process of the evolution from which fluid evolves from the timescale constrained by the lab experiment to the natural field time length, ranging from weeks to months of fluid residence time within a thick regolith.

Using these models, we extend our batch reactor results further in time through the numerical simulations (section 5.1) towards the timescales of fluid residence in the VMS (i.e. 526 hours or 22 days). By extrapolation, our simulations suggest that many features of the multi-component geochemical reaction network describing this system are still evolving and have yet to

stabilize even well beyond the first 150-200 hours (Fig. 12 below). This is particularly evident in the major cation ratios. For example, in the shallow and middle depth Ca/Na timeseries, the model continuously increases beyond the range of the experimental values as time progresses. In the deep Ca/Na timeseries, ion ratios even suggest that the initial trend towards higher values indicated in the experiments reverses at later time.

We also note that any minor inaccuracy in the kinetic parameters influences the rapid changes in solute composition in the first few hours of the batch reactions, and these inconsistencies are amplified in the ion ratios from the start of the simulation (Fig. 12). The initial evolution of these concentration ratios is also much more difficult to constrain due to the heterogenous nature of the material (i.e. effective reactive surface areas of minerals). However, the signal of the initial dilute concentration ratios is rapidly erased, and model values intersect the ratios observed in those cases where concentration change plateaued. By extending the simulations beyond the timescale limited in laboratory experimental setting, the models suggest fluids in the VMS continues to evolve further beyond the time span of the batch reactor experiments even though the rate of concentration changes decreases dramatically 20-50 hours after the start of the initial experiment.

The simulated ion ratios taken from our models show a clear increase from the 150 hours to 1000 hours for both the shallow and middle depths (Fig. 11). The increase of Ca/Na and Ca/Si ratios are due to the further enrichment of Ca in the fluid as small amounts of reactive minerals such as dolomite continue to dissolve. This result is also shown in both Ca/Si and Mg/Si ratios, where the shallow and middle depth values approach the deep ratio values with increased time in the first two simulations. In contrast, the deep model ratio values remain relatively small for both Ca/Na and Mg/Na (Fig. 11A) and for Ca/Si and Mg/Si (Fig. 11B). The consistency shown between the two ratio systems implies that given enough time for fluid to react with shallow and middle rock, we expect the fluid signature to evolve to that of the deep depth. However, the relatively small amount of change of the deep depth ion ratios through time imply that longer residence time affects the ion ratios less than those samples in the shallow and middle depth batch reactors. Thus, the solid composition exerts a principle control on the fluid solute concentrations. However, the variation of ratios at each depth (Fig. 11) in the field data suggests additional influences such as fluid transport pathways.

For fluid sampled at the shallow (1.5m) and middle (7.8m) depths by the VMS, the fluid residence time in this system would be about 180 and 950 days respectively if we assume a 3 m/yr flow rate. As suggested by the extension of our batch reactor models, we would expect the ratios to be more evolved in the natural system than the batch reactor experiments and reaching a ratio signature closer to that of the deep ion ratio. However, this is not the case, as demonstrated in the comparison between our experimental and field observations. Even though the batch reactor experiments only reach a duration of 150-200 hours, much shorter than that of fluid residence time even in the upper 18 cm of the vadose zone, the ion ratios of each respective depth are still close to the corresponding ratios observed in the VMS (Fig. 11). While bulk concentrations in fluid may change over time, the similar ratios indicate the water-rock interactions remain the same across the time scale of ranging from a couple of hundreds of hours (batch reactor experiments) to the hundreds of days (16 meters deep fluid).

Ultimately, the batch reactor simulations are able to reproduce the concentration of cations in close agreement to the batch reactor experiments over a short timescale, approaching a quasi-steady state. However, when these cations are recast as ion ratios, we see that they are much more sensitive indicators of geochemical evolution at longer timescales within this highly complex and heterogeneous chemical network. This short timescale fluid-rock interaction can be conceptually represented by the grey shaded box in Fig. 13A. In order to extend past the timescale that is feasible in such experimental designs, our numerical simulations replicate reactions occurring in the batch reactors to 1000 hours. However, these extended timescale simulations are isolated from the transport component of the fluid moving across the vertical subsurface in the vadose zone. In reality, fluid residence time increase is linked to fluid traveling deeper into the subsurface (Fig. 13B) and the transport component moves the fluid from the surface to progressively deeper regolith across the vadose zone and eventually into the aquifer. Our batch reactor experiments and models cannot simulate this effect of a changing regolith on the measured fluid values given these experiments were not performed with fluid transport. Therefore, the batch reactor experiments and models have provided insight into the evolution of fluid concentrations through time but are insufficient to explore the fluid evolution progressively through the vertical structure of the vadose zone. We thus expand these models to the depth-resolved structure of the vadose zone to explore the influences of coupled transport and reactivity.

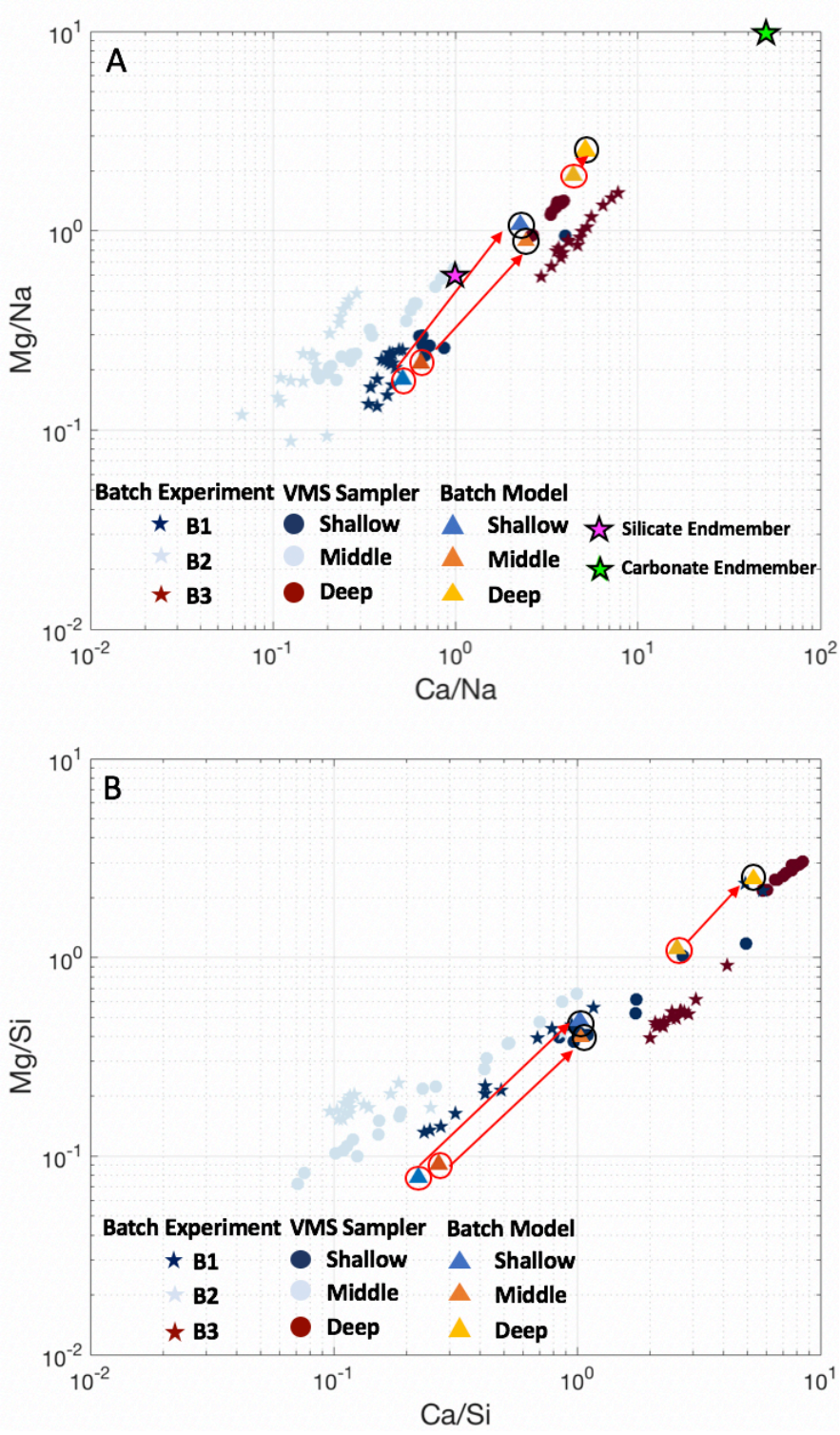

Figure 11. Panel A shows a compilation of VMS-B fluid, Batch reactor experiment, and Batch reactor model Ca/Na vs Mg/Na from shallow, middle, and deep depths. Panel B shows the associated samples for Ca/Si and Mg/Si system. VMS-B fluid ratios denoted by the circles are sampled from July 2016 to December 2017. Concentration ratios of the batch reactor experiments are denoted as stars. Batch reactor model ratios are denoted with triangles in a circle, where red circle indicates the ratio captured at 150 hours of simulation and black circles indicate ratios at 1000 hours of simulation. The red arrows are indicating the direction of movement of the model ratios in Ca/Na and Mg/Na ratio space from 150 to 1000 hours.

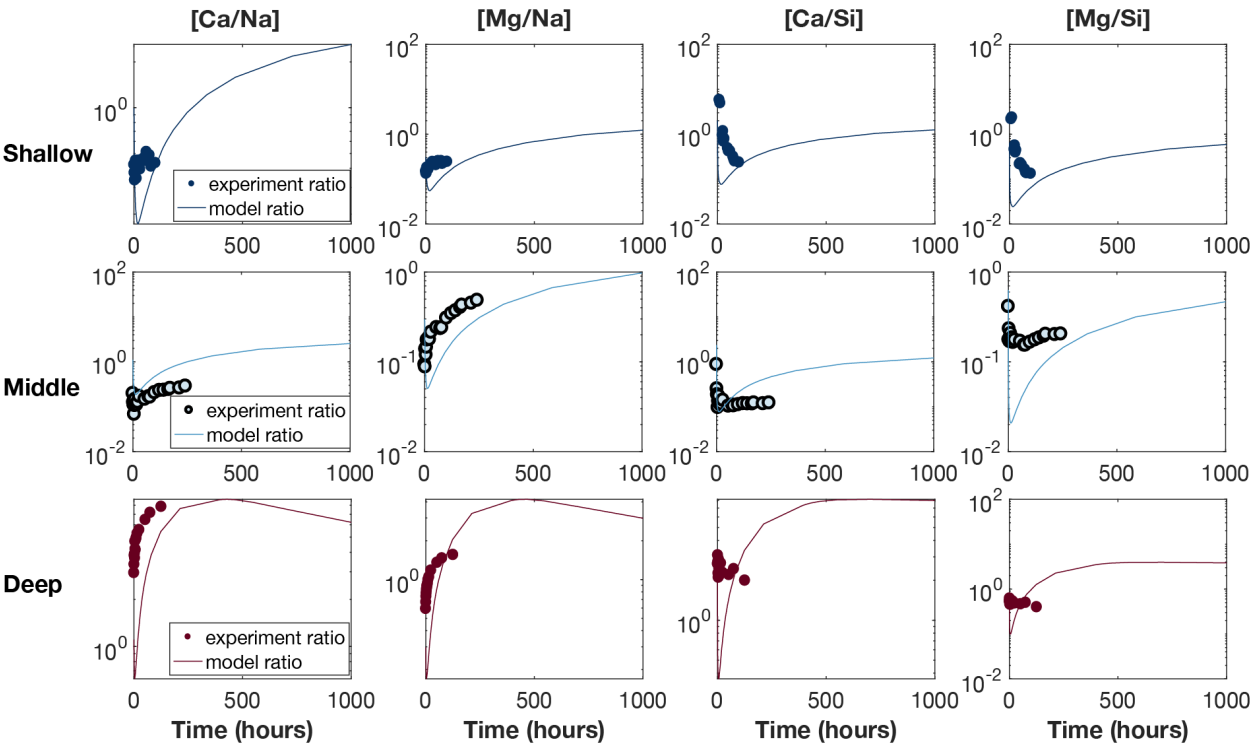

Figure 12. Shallow (row 1), middle (row 2) and deep (row 3) Ca/Na (column 1), Mg/Na (column 2), Ca/Si (column3), and Mg/Si (column 4) timeseries from the batch reactor experiments and associated models. Concentration and ratio values from experiment are denoted as points and model simulated concentrations and ratios are shown as lines. These simulations were carried out to 1000 hours (~41 days) for each of the shallow, middle, and deep batch reactor systems.

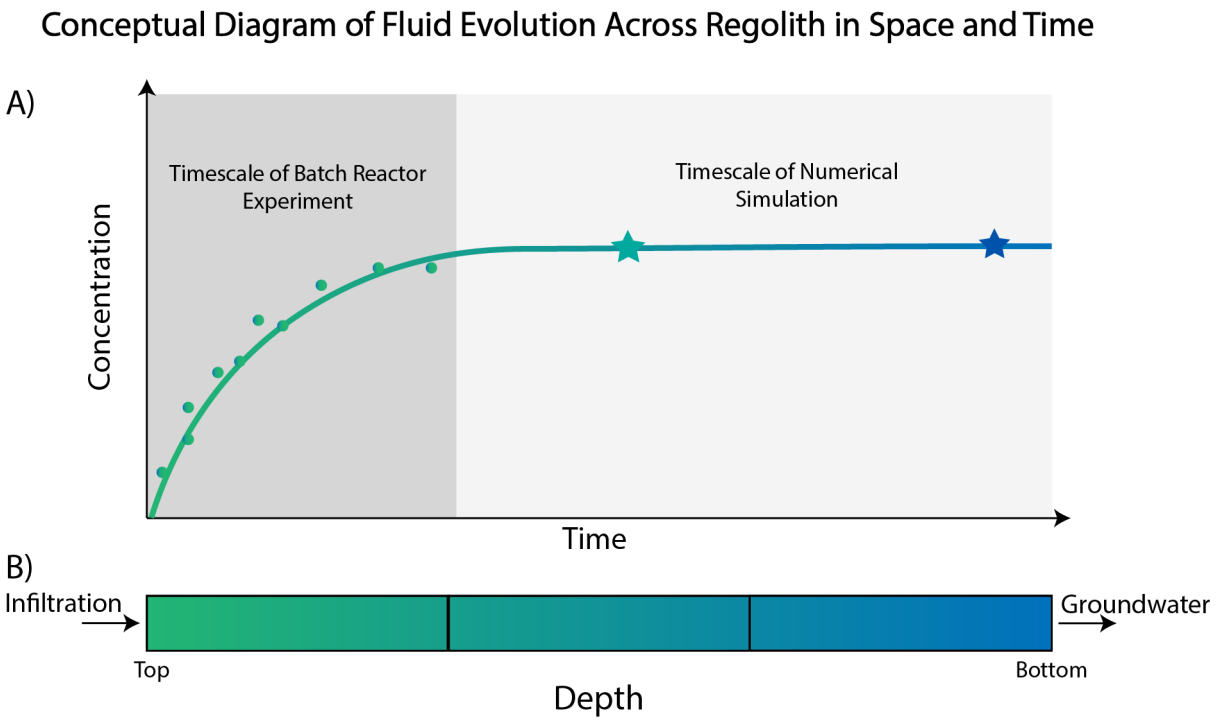

Figure 13. Conceptual model of the evolving solute concentration across the regolith profile. The dark grey shading in 13A highlights the timespan of solute concentrations observable in laboratory batch reactor experiments (on orders of days to weeks) and the light grey shading highlights the extended timescale to which numerical models can simulate fluid interactions beyond the time scale restricted to laboratory experiments. In panel B, shading of green to blue gradient represents the evolution of fluid from young (infiltration) to old (groundwater).

5.3 1D models of weathering regolith profile in shale hillslope

In total, the batch reactors provide an excellent method with which to isolate the geochemical reactivity of these systems, but converting these to the natural system requires consideration of the unique conditions of the open 1D system and sequential reactivity across the vertical profile. Using the multi-component reaction network constrained in the batch simulation, we accomplish this task through construction of a 1D reactive transport model to include transport effects of fluid and reactive gases across the profile. This section demonstrates the unique capacity of a reactive transport modeling framework to translate the chemical parameters constrained by a laboratory experiment into an open system context.

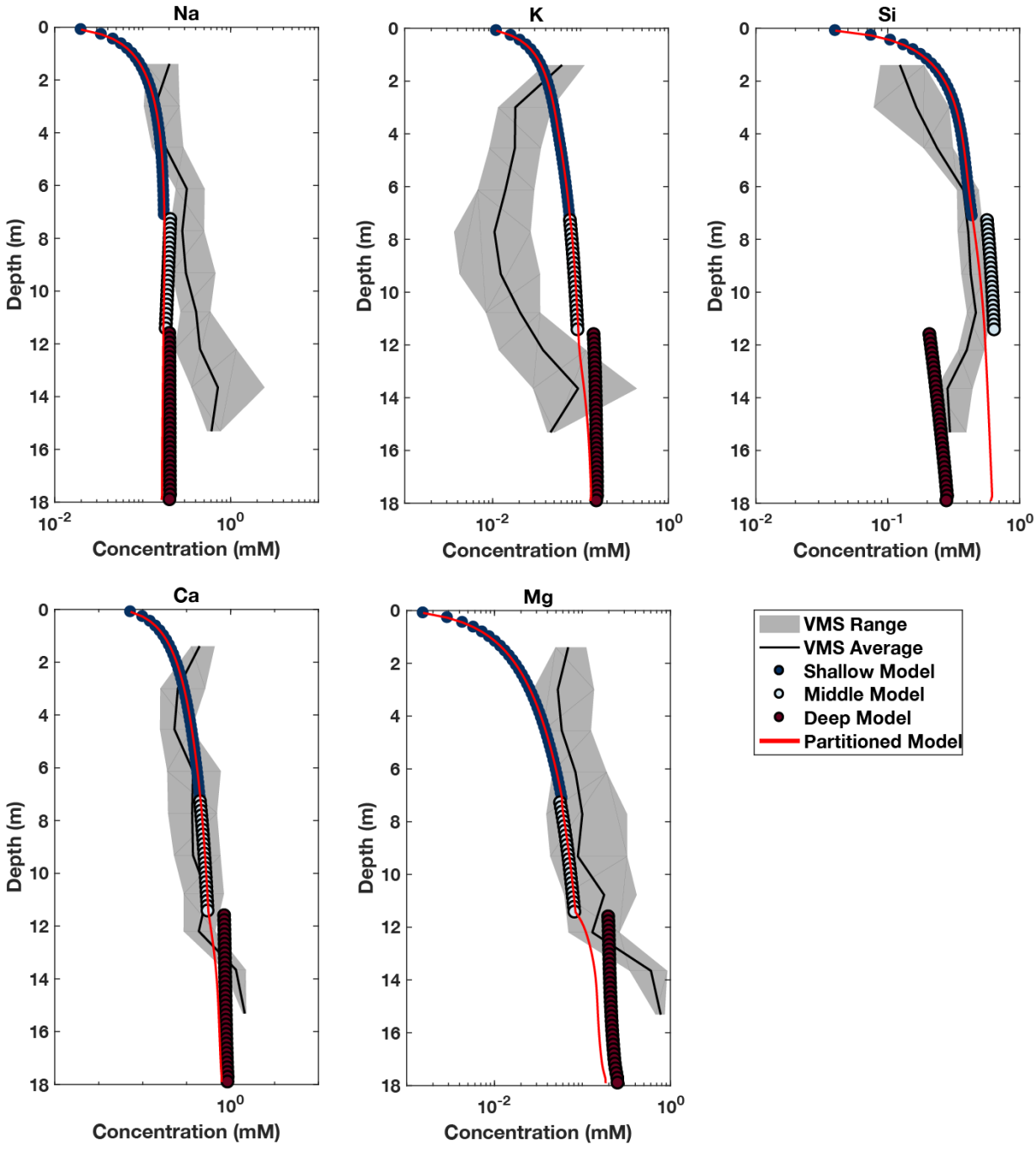

Figure 14. Concentration vs depth plots showing 1D model results from Shallow, Middle, and Deep models at the respective depths for Na, Si, K, Ca, and Mg. Grey shading shows the range of concentrations from VMS-B at various depths and the black line denotes the average concentration. The red line denotes model concentrations for a partitioned 1D domain model.

We want to test whether the fluid moving through progressively deeper layers with different mineral assemblages is important to the solute signature we observe. We built four 1D reactive transport models (Fig.3) where three were fixed with homogenous domains of shallow,

middle, and deep depth solid composition respectively and the fourth as a partitioned profile of solid composition. In Fig. 14, we see the concentrations of each of the five cations from the different models with its respective color markers. As expected, the partitioned model increases in concentrations synchronously with the Shallow model within the first 7 meters, since the mineral assemblage and fluid inflow are the same. The contribution of Na to the fluid is largely controlled by the dissolution of albite (chemical formula: $NaAlSi_3O_8$). Throughout the simulation, albite is unsaturated and thus continuously dissolving and releasing Na ions into fluid. The fluid from the Middle model is slightly higher in Na and Si concentration than the partitioned model.

The increase of Na ion attachment to the mineral surface replaced K on the surface sites and thus increases the concentration of K in the fluid. Additionally, we did not account for plant nutrient uptake of macronutrients which is likely to play an important role in the consumption of K in the subsurface (Nieves-Cordones et al., 2014; Pyo et al., 2010). Thus, we infer that the decrease of K with depth in the VMS-B is highly influenced by the vegetation uptake in the shallower depths and increases after the demand for plants decreases at greater depths. Below the shallow model, the concentrations are deviating from the prediction of the partitioned model. We observe that Na and Si concentrations of the middle depth model are slightly higher than that of the partitioned model. The deep depth model shows higher concentrations of Na, K, Ca, and Mg yet much lower concentrations of Si in comparison to the partitioned model. In essence, the partitioned model is creating a sequential evolution of fluid as it moves from shallow to deep solids, thus accounting for this unique progression which is unconstrained by isolated batch reactions.

5.4 Comparison with hindcasting 1D modeling framework

In most previous studies of the vadose zone, only the solid phase has been available for direct sampling and thus constraint of reactive transport models. These models are in turn limited to hindcasting efforts, in which an initially uniform bedrock is weathered to a modern profile and compared against the measured distribution (Buss et al., 2005; Molins & Mayer, 2007; Navarre-Sitchler et al., 2011; Reis & Brantley, 2017). Here, the unique instrumentation of the VMS allows us to capture the evolution of fluid and gases with depth and season. Because of this unique capability to observe fluid solute and gas patterns, we are able to constrain a reactive transport simulation over the current weathered gradient of bedrock with validation against the measured

concentrations of solutes generated as fluid moves through the profile. However, we also wish to maintain consistency such that the short timescale (50 years) simulations developed in our models also honor the same processes captured by more common weathering front development models. We test this consistency by extending the model run time out to the millennial timescale. At these longer timescales, tectonic uplift of the region becomes a relevant parameter. Uplift is estimated based on the Elder Creek incision rate of 0.2-0.4 mm/yr (Fuller et al., 2009) and 0.4 mm/yr is used in the current model.

Over a 2000-year simulation, we begin to see the development of reaction zones for albite, dolomite, and pyrite (Figure 15 A-C) in the depth profile. The albite dissolution front is the shallowest at approximately 2-4 meters (Fig. 15 A), while dolomite loss extends much deeper to approximately 12-14 meters (Fig 15 B). The pyrite oxidation front is located between those of albite and dolomite, from 4-6 meters (Fig. 15 C). The relative location of these fronts is reasonable given that dolomite and pyrite are much more reactive minerals than albite and thus their weathering fronts reach deeper into the Critical Zone. The predicted volume fractions at 2000 years for each of these dissolving minerals are comparable to those observed in the reported mineral fractions of the modern-day profile (Table 2. Regolith composition). Overall, the locations and extent of these primary mineral phases agree with the relative locations and extent of primary mineral loss observed in the solid phase distributions (Table 2) and thus our simulations extend to longer periods of time in a coherent framework.

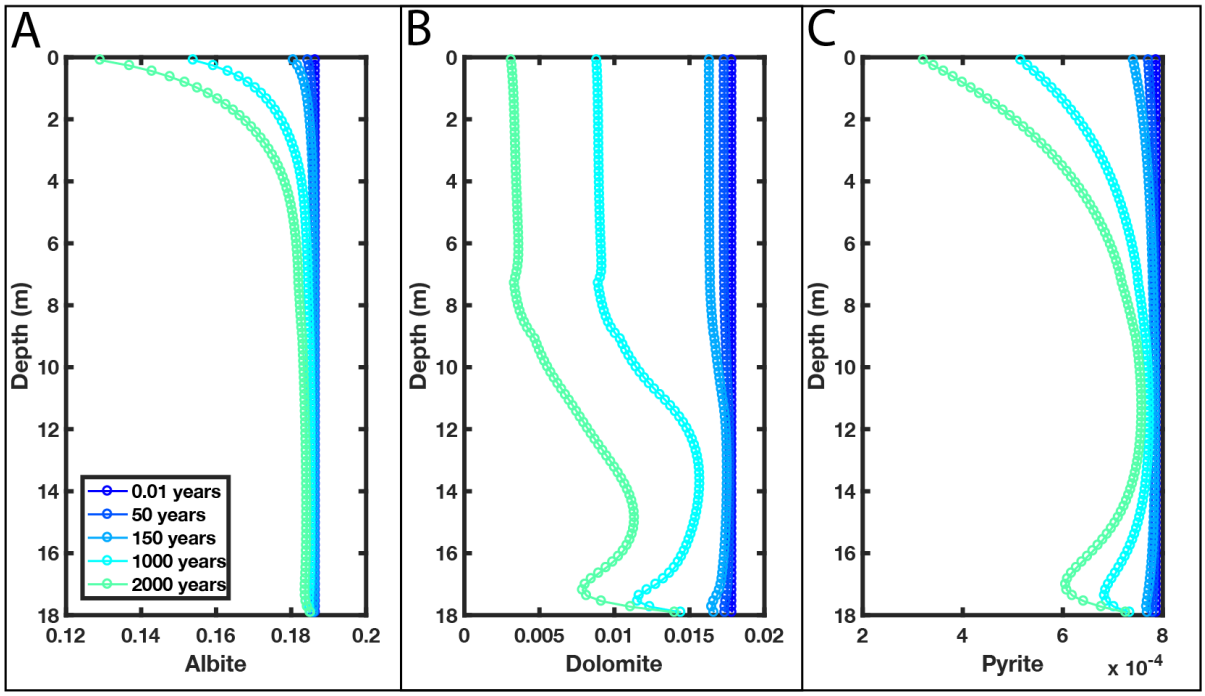

Figure 15. The volume fraction of albite (A), dolomite (B), and pyrite (C) with respect to depth from 0.01 to 2000 years of simulation. Model volume fractions include 20% porosity.

The argillitic bedrock underlying the ERCZO is composed of ~50% clay minerals. Constraint of the chemical reaction network involving these clay assemblages (kaolinite, illite, and smectite) is inherently more challenging (Blanc, Vieillard, Gailhanou, & Gaboreau, 2013; Kloprogge, Komarneni, & Amonette, 1999; Savage et al., 2007). In Fig 16, we show the model output for kaolinite, illite, and smectite profiles (Fig. 16 A-C). At 2000 years, we begin to see the development of a precipitation front for kaolinite in the uppermost 4 meters, reaching about 0.08 volume fraction at the surface. While the overall trend of the depth profile of kaolinite (Figure 16 A) is similar to what we expect from direct observation, the increase in volume fraction is large for just 2000 years of simulation. If the simulation is allowed to run for as long as the age of the hillslope (hundreds of thousands of years old), this rate is likely to overestimate the volume of secondary clay formation. This is likely associated with the co-weathering and co-formation of other intermediate clay phases such as illite (Figure 16 B) and smectite (Figure 16 C) that are highly nonlinear in this clay-rich profile. While we suspect clay formation and dissolution to be an important part of the weathering reactions in this shale bedrock, we are limited by the challenges of the complex thermodynamic and kinetic interplay of these metastable and sequential solubilities.

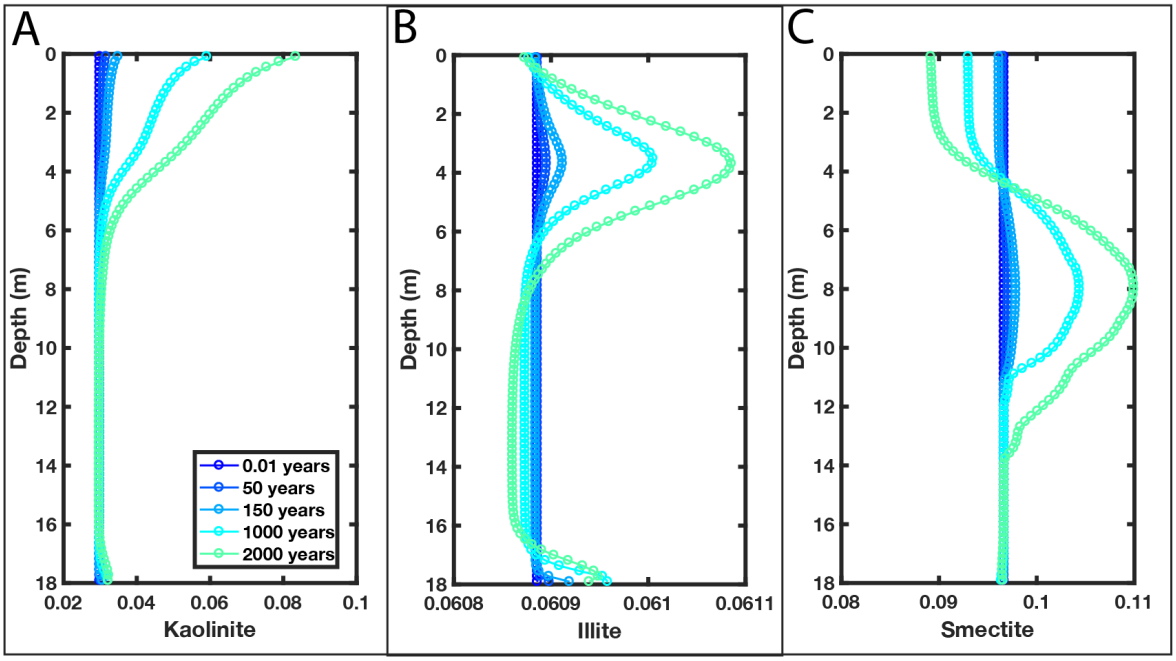

Figure 16. The volume fraction of kaolinite (A), illite (B), and smectite (C) with respect to depth from 0.01 to 2000 years of simulation. Model volume fractions include the 20% porosity.

In total, while the scope of this paper is focused on a much smaller timescale emphasizing fluid evolution through the present-day regolith, the longer hindcasting simulation of weathering profile formation shows consistent behavior reflected in the development of anticipated trends for most mineral profiles. We acknowledge the feedbacks between contemporaneous clays are complex, but to first order, we observe kaolinite accumulating at 2000 years of simulation in agreement with our measured values (Table 2). The approximate reproduction of these mineral profiles from unweathered bedrock to their present state is thus consistent with the present model architecture, but a complete development of such a model is beyond the scope of the current study.

5.5 2D fracture model

The general trends of the 2D flux-weighted average concentrations for Na, Si, K, Ca, and Mg are very similar to the profiles from the 1D partitioned model (Fig. 17). The concentrations of the 1D partitioned model are generally slightly higher than the 2D model throughout the profile. This behavior is the result of representing the fracture in the 2D simulation using a higher porosity and thus lower mineral volume fraction in this subset of the domain. In the fracture model, we estimate the flow velocity to be about approximately 100 times faster than flow within the matrix. This decreased mineral volume fraction creates an attendant loss of mineral surface area, which

propagates into the average mineral surface area available for reactions across any depth transect in the 2D system. This diminished surface area results in lower concentrations of cations in solution. For example, the difference in surface area of albite per volume rock at a given depth is 91.34 $\frac{m^2}{m^3}$ in the 2D domain, relative to 96.97 $\frac{m^2}{m^3}$ in the 1D model.

Furthermore, we note that a smaller (and possibly more realistic) aperture to matrix ratio for the fracture appropriate for shales (Gale et al., 2017) would be expected to produce an even smaller distinction between the 2D flux weighted average and the 1D model. Thus, the simplification of the 1D domain for this highly fractured system does not appear to create significant differences in behavior for the simulation of major cations in solution across the weathering gradient.

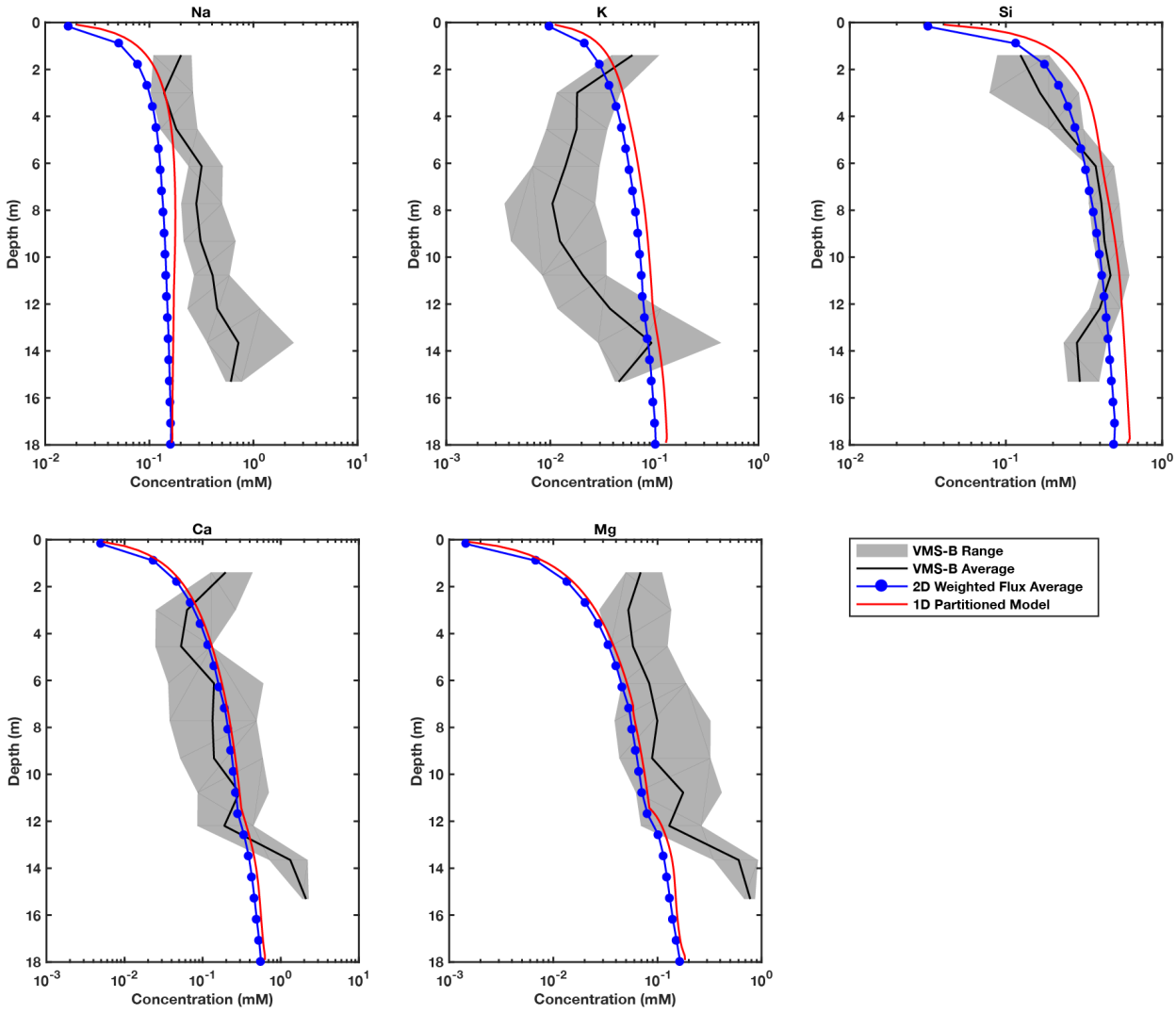

Figure 17. Comparison between weighted flux average concentrations from the 2D fracture model (blue) and 1D model (red) depth profiles for Na (A), Si (B), K (C), Ca (D), and Mg (E). The black line illustrates the average measured concentration and the gray shading indicates the minimum and maximum range observed. Both simulations were run to 50 years.

5.6 Significance of cation exchange

A recent study reported the lithology and groundwater chemistry of the ER-CZO over a four-year period from 2009 to 2012 (Kim et al., 2014). They presented a long-term high-frequency record of groundwater evolution along a transect defined by three vertically drilled wells located upslope, midslope, and downslope (Figure 1). The co-variation of the major cation concentrations (Ca, Mg, Na, K and Si) were reported in relation to the rise and fall of the groundwater table. In the mid and upper slope wells, they observed a decrease in cation concentrations in groundwater

when the water table was rising and increased concentration during recessions. Notably, Si concentrations displayed the opposite behavior where a high-water table correlated with high Si concentrations and a low water table exhibited low Si concentrations. When the groundwater table is elevated, fluid flow paths to reach the aquifer are shorter than when the groundwater table is low. Kim et al., (2014) hypothesizes that in this shorter fluid flow path, cation exchange processes facilitated by the presence of high pCO_2 (and thus excess proton in fluid) are the principal driving mechanism generating solute concentrations. The equilibrated cation-exchange reactions yield relatively dilute cation concentrations while preferential dissolution of amorphous silica associated with high carbonic acid caused the uniquely elevated Si signature. When the groundwater table is low, infiltration travels across a thicker vadose zone to reach the aquifer. This thicker vadose zone and hence longer flow path, allows fluid to approach equilibrium with relatively reactive minerals, principally calcite and secondary clays, while continuing to dissolve primary minerals such as albite. While the upper and midslope groundwater concentrations are tied to the rise and fall of the groundwater table, the downslope well exhibits relatively little variation throughout the year.

Furthermore, Kim et al. (2017) proposed that this vadose zone cation-exchange controls concentrations when fluid is relatively dilute at high flow rates in Elder Creek, while during low flow, fluid reaches thermodynamic equilibrium with the clays. Thus, the stream fluid maintains a relatively low fluctuation in major solutes and Si concentrations, displaying chemostatic behavior over a wide range of stream discharge. As groundwater flows laterally and down gradient to discharge into Elder Creek fluid degases at springs and drives calcite precipitation, keeping Ca concentration in the stream at a relatively low quantity compared to groundwater.

Kim et al. (2014, 2017) inferences regarding the role of cation exchange were based on PHREEQC (Appelo and Postma 2005) simulations of the fluid concentrations equilibrated with cations on surface exchanger sites as a function of pCO_2. PHREEQC supports several methods of implementing cation-exchange reactions between fluid and surface exchange sites. Amongst these choices, Kim et al (2014) specified a fixed mass of solutes available on surface exchanger sites and allowed the cations present on these surface sites to be supplied into the fluid as a result of substitution by excess protons produced through a fixed high pCO_2 condition. In tandem with this proton substitution, elevated carbonic acid also drove the dissolution of an amorphous silica phase which was specifically designed to release Si into solution. This approach predicts an associated fluid concentration, assuming instantaneous equilibration between fluid and surface sites.

However, this treatment overlooks the necessity for replenishment of cations on the mineral surface which must occur through some pathways of mineral dissolution or contribution from infiltrating water. Additionally, the influences of high pCO_2 and pH is prescribed and not generated via organic carbon respiration.

Thus far the simulations developed in the present study for both the batch reactions and through-flowing VMS profiles have included direct water-rock reactions (dissolution and precipitation) as well as cation exchange (Section 5.2-5.5) of the vadose zone profile. Using this calibrated model, we can to test the relative influence of this solute regulating pathway by removing cation exchange reactions in the 1D partitioned and 2D fracture models (Fig. 18). The cation exchange reactions (Table 4) result in preferential attachment of Mg and Na to exchanger site surfaces and the corresponding release of K and Ca. These exchange pathways do not directly influence the Si concentrations as these conditions largely support the formation of uncharged $SiO_{2(aq)}$ or silicic acid ($H_4SiO_{4(aq)}$) in solution. However, because of preferential attachment of Na to the surface sites, the corresponding decrease of Na in the fluid drives slightly greater dissolution of albite and thus results in higher Si concentrations (Fig. 18 A and C). Thus, ion-exchange influences mineral reactivity indirectly though the redistribution of cations between surface and fluid.

In total, the results of the 1D model comparing the complete simulation and the case in which ion exchange is simply removed suggests that the role of cation exchange is relatively minimal in the general concentration profiles. However, this is not a direct evaluation of the Kim et al (2014) model, in that our CrunchFlow simulations do not treat ion exchange in the same way as the PHREEQC model. Instead of equilibration of dilute fluid with a fixed (and thus potentially infinite) mass of ions on the exchanger site, CrunchFlow uses the initial fluid solute concentrations to calculate the corresponding mass on the surface in equilibrium with the fluid on the surface sites at the beginning of the simulation. Subsequent shifts in solute composition then change the distribution of ions on the surface sites and may even eliminate the presence of a given sorbed ion as in the case of a contaminant. Therefore, in order to simulate the 'fixed mass' on surface exchanger sites as implemented by Kim et al. (2014) using PHREEQC, we return to the 2D domain to create a system in which the matrix facilitates diffusion of solutes to the fracture as a result of the combination of dissolution/precipitation of minerals and ion-exchange from within the matrix

rock as a source of solute replenishment and redistribution of cations across the interface of fast and slow flow paths.

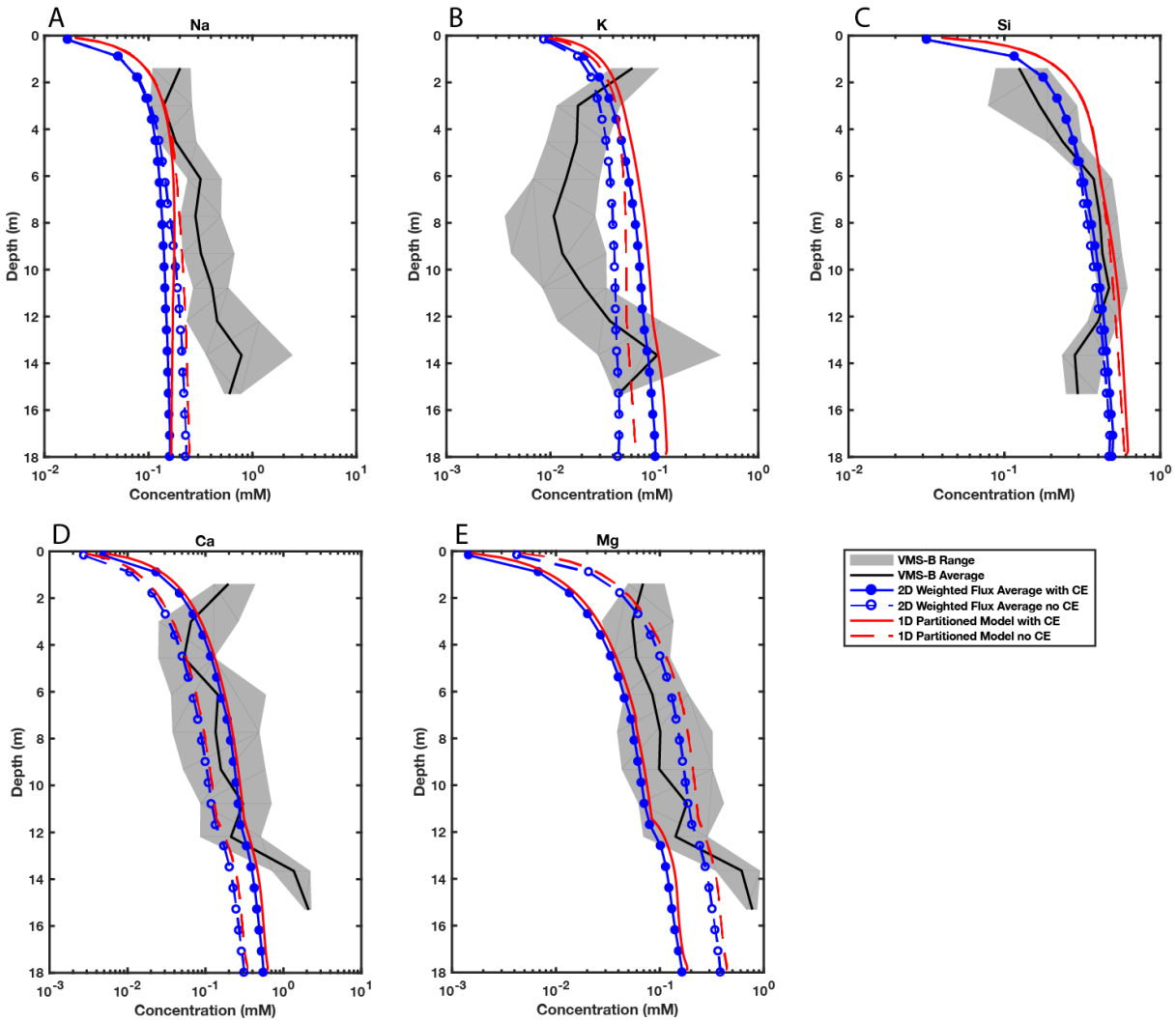

Figure 18. These plots show concentrations with cation exchange (CE) reactions (solid lines) in simulation and without (dashed lines) for the 2D (blue) and 1D (red) model respectively. Blue circles are depths at which the 2D fracture model weighted flux concentrations are calculated and blue dashed and solid lines are interpolation between these points.

To do this, we fixed the fracture domain with the same low porosity (section 5.5) but containing only effectively non-reactive quartz. In contrast, the matrix rock adjacent to the fracture retains its original porosity (0.2) but uses a decreased permeability 3 orders of magnitude. This low porosity and permeability results in effectively negligible flow rates in the matrix rock relative to the fracture. The matrix rock still holds the suite of reactive minerals used in the previous models. Fluid within the matrix thus reaches much higher solute concentration due to the longer

residence times. In contrast, fluids within the fracture travels much faster through an effectively non-reactive medium. Therefore, fluid draining the base of the domain is almost entirely sourced from the fracture, and the solute content of that fluid is almost entirely a result of diffusion and ion exchange between the fracture fluid and the more concentrated fluid of the adjacent matrix. The resulting fluid concentrations in the fracture are thus effectively in diffusion-regulated communication with a large reservoir of equilibrated solutes and associated exchangeable surface sites, resulting in a closer approximation to the 'infinite' reservoir of exchangeable ions created by the fixed surface site composition used in the Kim et al (2014) PHREEQC models. Another important difference is that our model allows pCO_2 levels to evolve as a result of organic carbon respiration instead of prescribing a fixed partial pressure value. Thus, our model's high pCO_2 content and its associated reactivity are due to the direct influence simulated by oxidation of organic carbon, an important process known to contribute to reactivity in the deep subsurface (Hasenmueller et al., 2017).

Ca, Na, K, Mg, and Si concentrations in our adjusted 2D fracture fluid are 0.076 mM, 0.026 mM, 0.040 mM, 0.020 mM, and 0.085 mM at the base of the domain, respectively (Table 4 Case A). In contrast, these concentrations in the matrix are 0.524 mM, 0.127 mM, 0.095 mM, 0.151 mM, and 0.270 mM respectively, approximately 3-8 times higher than that of fracture fluid (Table 4 Case A). As a point of comparison, the 2D model presented earlier (section 5.5) where reactive minerals were present in both the fracture and matrix sub-domains produced flux-weighted fluid concentrations that are higher overall (Table 4 Case B). When mineral reactivity is effectively removed from the fracture, such that solute increase can only occur as a result of ion exchange and diffusion, the concentrations are much lower than observed concentrations from the VMS in the range of depth where groundwater is encountered. Therefore, this suggests that while cation exchange may contribute to the distribution of solutes observed in vadose zone fluids, this process cannot create a net increase in concentration of the same magnitude as the combined effects of weathering reactions, and thus serves a supporting role in the generation of solutes as a result of mineral dissolution. Furthermore, the combined effect of weathering and solute diffusion serves as a reliable source of solutes generation for replenishing surface sites while cation-exchange influences the distribution of this existing reservoir.

Table 4. Flux weighted concentrations of Ca, Na, K, Mg, and Si from 2D models at the bottom of the domain.

	Case A**			Case B***		
	Fracture*	Matrix*	Overall*	Fracture*	Matrix*	Overall*
Ca	0.076	0.524	0.208	0.179	0.923	0.559
Na	0.026	0.127	0.056	0.120	0.200	0.161
K	0.040	0.095	0.056	0.059	0.145	0.103
Mg	0.020	0.151	0.058	0.057	0.270	0.165
Si	0.085	0.270	0.139	0.285	0.692	0.493

* Concentrations in mM

**Chemical reactions, diffusion, and cation-exchange in matrix domain. Cation-exchange and diffusion only in fracture domain

***Chemical reactions, diffusion, and cation-exchange in both fracture and matrix domain (Figure 5)

5.7 Mineral solubility

The second principle Kim et al. (2014, 2017) hypothesis suggested that groundwater is undersaturated with respect to primary minerals but has reached equilibrium with more reactive carbonates and clays. Here, we use the Na-feldspar stability diagram to determine fluid saturation with respect to mineral(s) found within the VMS core. The ion ratio of Na/H+ vs the concentration of Si in the VMS fluids and our 1D partitioned model are plotted on a solubility field (Fig. 19). This exercise illustrates the evolution of the VMS fluid ratios in this stability space, and it is clearly evident that the fluids are evolving towards the albite stability field with increasing depth. However, even the deepest samples are still within the kaolinite stability field. Thus, our direct model of the vadose zone structure and reactivity supports the earlier Kim et al. (2014) hypothesis that fluid within the vadose zone remains undersaturated with respect to primary minerals such as albite and becomes oversaturated with some clays. Furthermore, our reactive transport model (purple points in Fig. 19) also shows strong agreement with the evolution of the VMS fluids. Thus, we can verify that the model is capturing the major processes influencing mineral saturation. On the other hand, Kim et al. (2014) also hypothesized that the fluid deep in the subsurface reached thermodynamic equilibrium with reactive minerals (i.e. calcite). Our model indicates that fluids in deeper intervals are saturated with respect to calcite but remain undersaturated with respect to dolomite. Given the increase in both Mg and Ca concentrations at deeper intervals of the vadose zone, this would support that the carbonate mineral in this system is closer to that of dolomite than

that of pure calcite. Therefore, this would suggest that while fluid might be in equilibrium with clay minerals, high Ca and Mg concentrations are sustained by the continuous dissolution of dolomite even at the deepest depths and have yet to reach equilibrium. Furthermore, the saturation with respect to calcite in the lower depths of our 1D reactive transport model supports Kim et al. (2017) hypothesis of calcite precipitation when groundwater exits the subsurface into Elder Creek.

While Kim et al. (2014) hypothesized that dissolution of amorphous silica is the source of high Si concentration during the rise of the water table, direct testing of this inference is difficult to reliably quantify and justify given the need for large amounts of amorphous silica in the subsurface which is not detected in the XRD analysis of regolith. The lack of evidence for amorphous silica in the mineral assemblage quantification implies that this is unlikely to be large source of reactant for reactivity. Instead, we have implemented parallel rate laws (Mayer et al., 2002; Wen & Li, 2018) for the dissolution of albite and microcline associated with pH dependence. In this sense, at lower pH, additional albite and microcline will be dissolved to increase Na and Si concentrations. Using this approach, we are able to reproduce a very robust concentration profile for Na and Si in the 1D model without amorphous silica. When we omit this pH-dependent rate law, Na and Si concentrations decrease by an order of magnitude relative to our observed concentrations in the VMS. In total, these parallel rate laws are necessary to produce Na and Si concentrations in the range observed in VMS and we suggest this approach is more robust than invoking large quantities of an amorphous phase which is difficult to constrain and only impacts Si. Furthermore, our reactive transport simulations show that amorphous silica is consistently undersaturated in our system, thus further supporting that clay precipitation/dissolution is the dominant control on dissolved silica concentration.

Finally, Kim et al., (2014) hypothesized that the precipitation of metastable aluminosilicates (i.e. kaolinite) are responsible for decreased Si concentrations when the water table is low. In our reactive transport model, we did not include gibbsite as a mineral phase because it was not detected in the XRD analysis of the recovered regolith. The model shows that Si concentration isn't simply limited by the precipitation of kaolinite but rather a complex network of secondary clays forming and dissolving while albite remains undersaturated. Clay minerals such as chamosite and smectite become saturated and form at depth while kaolinite is saturated in the top half of the domain but undersaturated in the bottom half. Illite behaves similarly to kaolinite but is only undersaturated in the top 2.6 meters. In total, we suggest that while precipitation of

secondary aluminosilicates (predominantly kaolinite) is part of the process that lowers Si concentration in the deep vadose zone, the overall concentration of silica is controlled by interplay between dynamics of the complex clay network and the dissolution of albite.

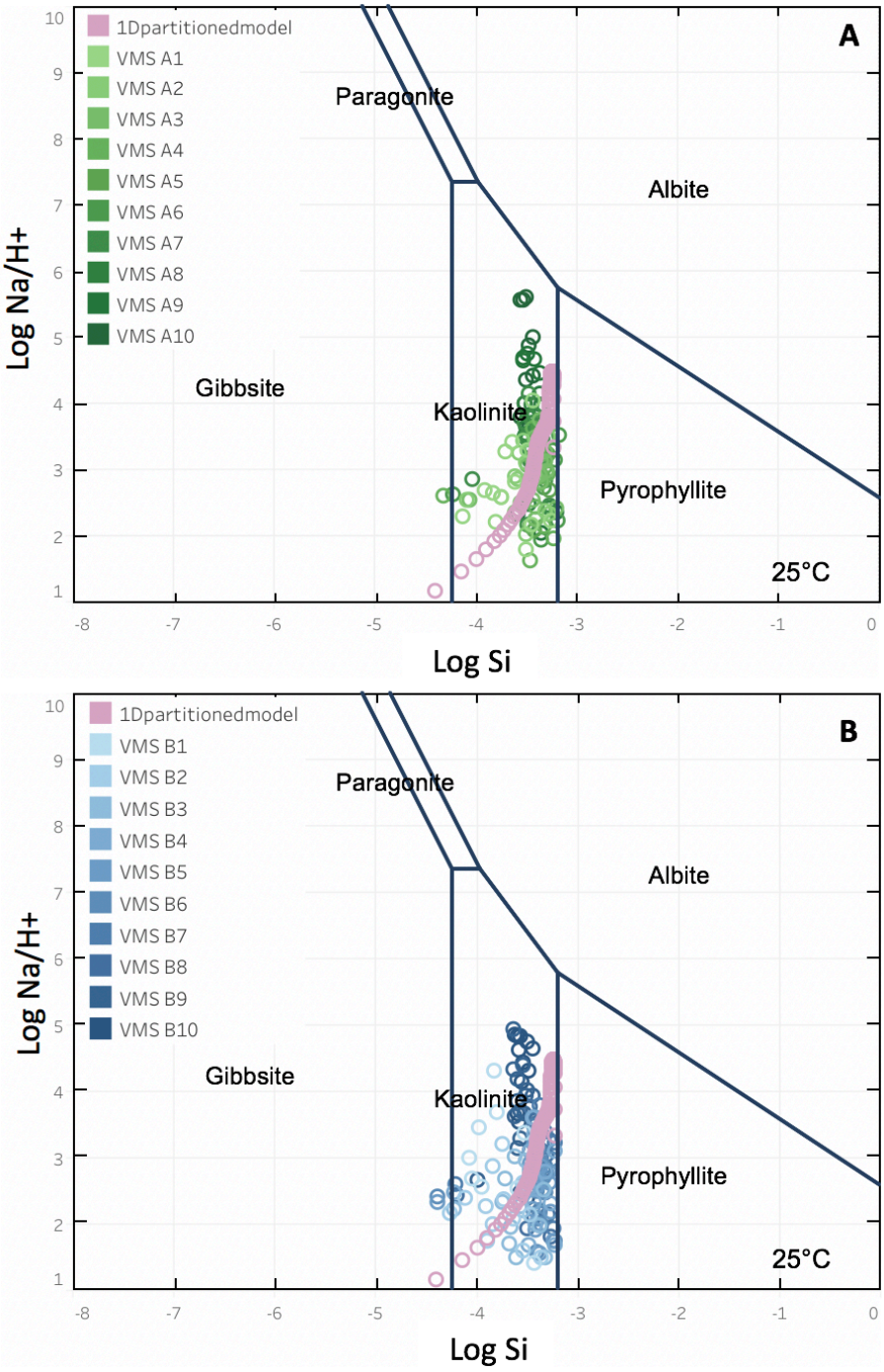

Figure 19. Stability diagram of albite and associated clay minerals for VMS-A (green) in panel A, VMS-B (blue) in panel B, and results from 1D partitioned model simulation (purple) in both diagrams.

5.8 Addressing variability in flow rate

Flow rates through the vadose zone are extremely difficult to directly quantify. Inherent estimation of pore fluid connectivity is difficult and large variability also occurs in both tree canopy interception and evapotranspiration of precipitation depending on the density of trees and season. For all models presented thus far, we have assumed an average annual precipitation of (2000 mm to 2500 mm), a corresponding IT of (400 mm) and ET of (600 mm). While we have estimated the overall porosity is 20%, the assumption of the component of that porosity that is fluid saturated is difficult to constrain. However, we recognize that fluid flow through the vadose zone is neither uniform through time (dry vs. wet season) or space (across the vertical profile). In our present models, the value of 3 m/yr is likely on the low end of flow rates even for the estimated distribution of precipitation, ET and IT, in that the component of porosity that is connected and available for flow is likely much lower than the overall estimated porosity. To explore the effects of variability of flow during different seasons resulting from changes in fluid saturation, we adjusted the φ_{flow} from our original 50% to approximately 5%, arriving at an estimated velocity of roughly 20 m/yr. Here, we test the partitioned 1D model over a range of fluid infiltration rates to consider the associated sensitivity of our results. We observe that an increase in fluid flow rate from 3 to 20 m/yr decreases solute concentrations by 25% or greater, uniformly in K, Si, Ca, and Mg (Fig. 20) after fifty years of simulation. At a flow rate of 20 m/yr, the solute concentrations decrease even further to less than about 30% of the concentrations at the flow rate of 3 m/yr. Sodium concentrations are 60% lower at the surface but the difference diminishes with depth. Notably, the lack of variation across flow rates in the deep Na concentrations even though albite is undersaturated in the model offers one example of the role of ion exchange. For sodium, the influence of ion-exchange is relatively stronger than the other ions, and the corresponding variation is dampened as a result of replacement from surface sites.

The results of this sensitivity test illustrate a dynamic range of concentrations depending on the fluid flow rate, and large variability in factors contributing to the fluid flow (i.e. fluid availability and permeability). The simulations conducted thus far have been at a relatively slow value of 3m/yr and produce results that are closest to the observed data in the VMS. In contrast higher flow velocities (10 and 20 m/yr) generally result in concentrations that are too low. This suggests that while flow rate may fluctuate widely over shorter periods (days), the effective average flow rate at the yearly resolution is close to that of 3 m/yr. Furthermore, the VMS profiles

show much less concentration variability over season than over depth intervals, even though flow rate must be slower in dry summer months and faster in wet winters. The comparable concentrations at each depth through season implies that fluid must reach steady concentration relatively quickly with the rock to produce similar concentrations across this range of flow. This lends support to the argument that solute concentrations in our system is primarily influenced by the chemical reactivity network and the progression of contact with a regolith profile which transitions from highly weathered at the surface to unweathered at depth.

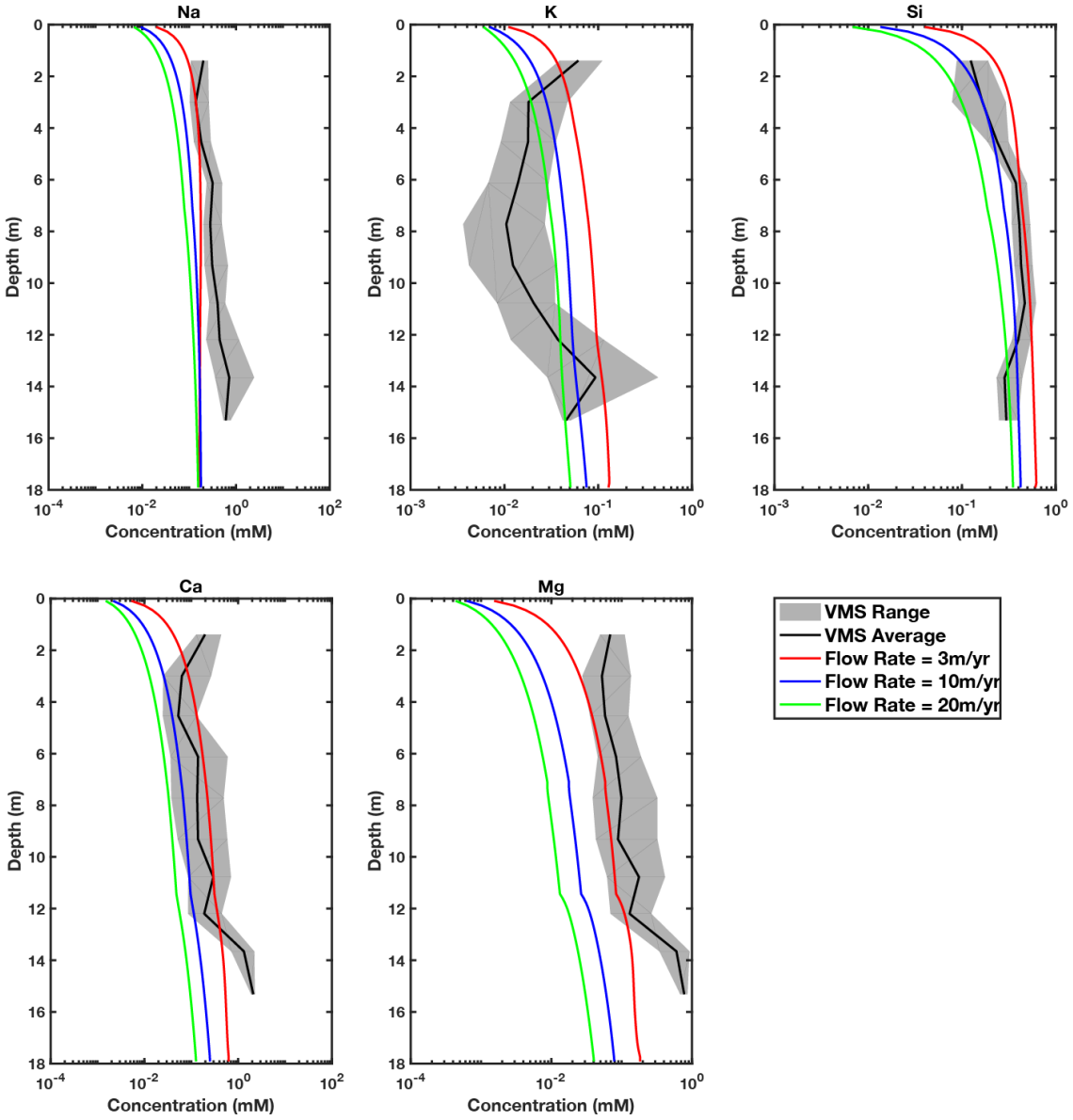

Figure 20. Here we shows 1D simulations with flow rates at 3 m/yr (red), 10 m/yr (blue), and 20 m/yr (green) for Na, K, Si, Ca, and Mg at 50 years of fluid flow.

CHAPTER 6: CONCLUSIONS

Leveraging the unique vadose zone sampling capabilities of the VMS, we have generated a novel high resolution spatio-temporal geochemical dataset of the fluid draining through a vadose zone profile. We further isolated relative effects of transport and water-rock reactions through a series of closed system batch reactor experiments. While the solute concentrations of these batch reactors are generally much lower compared to the that of fluid in the natural system as a result of the shorter time scale and unique water-rock-gas ratio and pCO_2, the ion ratios of these experiments agreed closely with the vadose zone samples. This suggests that the fluid-rock interactions within our vadose zone profile reflect the progressive, systematic lithological changes from the most chemically weathered material at the surface to the least weathered bedrock at depth.

We developed a quantitative numerical simulation of the coupled multi-component chemical reactions and fluid and gas phase transport across this regolith in both 1D and 2D frameworks. Importantly, these simulations employed previously established kinetic and thermodynamic parameters and were not simply fit to the present observations. More importantly, this model incorporates reactive gases (CO_2 and O_2) in the chemical reactivity network via organic carbon respiration and thus allows the dynamic evolution of gas profiles to directly affect the extent of chemical reactivity. In our 1D models, we see the partitioned profile of weathered regolith exerts significant influence on the silicate weathering of albite, illustrating substantial discrepancy between the 1D "deep homogenous" and "partitioned" model in Si concentrations at 12 meters and below (Fig. 14). While fluid residence time dictates the extent to which equilibrium is reached, the influences of solute evolution from the progressive movement across this weathering gradient is subtle and often excluded from the conceptual model of chemical weathering on Earth's surface. Our work here suggests that these subtle differences are important to accurately predict the solute concentrations in the vadose zone and consequently the weathering fluxes from the vadose zone.

We have also tested the effects of fracture influence on solutes by reducing the porosity and increasing the permeability of a subsection of the domain in a 2D framework to simulate fracture behavior. The flux-weighted averages across the 2D domain are slightly lower compared to that of the 1D model due to the lowered availability of mineral reactive surface areas (i.e. albite) within the higher porosity fracture domain. This implies that the explicit pattern of the fracture system within the regolith may not need to be represented in order to accurately predict solute evolution, at least for these major ions. At the current resolution, the representation of the fracture

network as simply a higher porosity is sufficient in our reactive transport models to predict solute evolution and concentration profiles.

Finally, we used the models to explore whether or not ion-exchange is a dominant process by which fluid gains solutes. We reduced the effective mineral reactivity in the fracture domain to non-reactive quartz while the matrix domain remains fixed with a higher reactive mineral fraction. The results show that fluid solute concentration without the reactive minerals in the fracture is ~30%-75% lower than that of the its counterpart. We found that while ion-exchange can redistribute solutes throughout the profile, its effects appear to be secondary to that of chemical weathering. Furthermore, we found evidence through both our observed data from the VMS and numerical simulations indicating that the fluid in this shale bedrock is continuously undersaturated with respect to albite but in equilibrium with some clays, in agreement with observations of Kim et al. (2014, 2017) based on groundwater samples from 2009-2011. However, we suggest that the clay network at this shale bedrock system is more complex than originally proposed by Kim et al. (2014). The saturation state of several clays (i.e. kaolinite, illite, smectite, chlorite) in addition to the influence of continuously dissolving albite are key in controlling Si concentrations.

Lastly, sensitivity tests of high flow rates (10 and 20 m/yr) resulted in much lower solute concentrations than the models run at 3 m/yr. While the estimate of 3 m/yr may be lower than what could be expected during rainy seasons, the concentrations produced at this flow rate is closest to what is observed in the VMS. This strongly suggests that the effective flow rate for the yearly resolution is not the principle factor governing solute concentrations. Given the small variability of solutes with season compared to the larger variations with depth, the model suggests that chemical reactivity is reaching steady state at respective depths even at fast flow rates. In total, this suggests that chemical reactivity across this weathering gradient is of greater influence to observed solute generation than that of residence time. This subtle difference accounting is therefore crucial to consider when trying to accurately constrain solute fluxes from the vadose zone, where little hydrologic and geochemical information was previously known.

CHAPTER 7: REFERENCES

Alekseyev, V. A., Medvedeva, L. S., Prisyagina, N. I., & Balabin, A. I. (1997). <Dissolution rates of alkali feldspars.pdf>, *7037*. https://doi.org/10.1016/S0016-7037(96)00405-X

Anderson, S. P., & Dietrich, W. E. (2001). Chemical weathering and runoff chemistry in a steep headwater catchment. *Hydrological Processes*, *15*(10), 1791–1815. https://doi.org/10.1002/hyp.240

Anderson, S. P., von Blanckenburg, F., & White, A. F. (2007). Physical and chemical controls on the critical zone. *Elements*, *3*(5), 315–319. https://doi.org/10.2113/gselements.3.5.315

Banks, E. W., Simmons, C. T., Love, A. J., Cranswick, R., Werner, A. D., Bestland, E. A., … Wilson, T. (2009). Fractured bedrock and saprolite hydrogeologic controls on groundwater/surface-water interaction: A conceptual model (Australia). *Hydrogeology Journal*, *17*(8), 1969–1989. https://doi.org/10.1007/s10040-009-0490-7

Beckingham, L. E., Mitnick, E. H., Steefel, C. I., Zhang, S., Voltolini, M., Swift, A. M., … Depaolo, D. J. (2016). ScienceDirect Evaluation of mineral reactive surface area estimates for prediction of reactivity of a multi-mineral sediment. *Geochimica et Cosmochimica Acta*, *188*, 310–329. https://doi.org/10.1016/j.gca.2016.05.040

Blake Jr., M. C., Jayko, A. S., & McLaughlin, R. J. (1985). Tectonostratigraphic terranes of northern California. In *Tectonostratigraphic terranes of the Circumpacific region* (Vol. 1, pp. 159–171). Circumpacific Council for Energy and Mineral Resources. Retrieved from http://pubs.er.usgs.gov/publication/70197684

Blanc, P., Vieillard, P., Gailhanou, H., & Gaboreau, S. (2013). Thermodynamics of clay minerals. *Developments in Clay Science*, *5*(October 2017), 173–210. https://doi.org/10.1016/B978-0-08-098258-8.00006-7

Brantley, S. L., Goldhaber, M. B., & Vala Ragnarsdottir, K. (2007). Crossing disciplines and scales to understand the critical zone. *Elements*, *3*(5), 307–314. https://doi.org/10.2113/gselements.3.5.307

Buss, H. L., Bruns, M. A., Schultz, M. J., Moore, J., Mathur, C. F., & Brantley, S. L. (2005). The coupling of biological iron cycling and mineral weathering during saprolite formation, Luquillo Mountains, Puerto Rico. *Geobiology*, *3*(4), 247–260. https://doi.org/10.1111/j.1472-4669.2006.00058.x

Dellinger, M., Gaillardet, J., Bouchez, J., Calmels, D., Louvat, P., Dosseto, A., … Maurice, L.

(2015). Riverine Li isotope fractionation in the Amazon River basin controlled by the weathering regimes. *Geochimica et Cosmochimica Acta*, *164*, 71–93. https://doi.org/10.1016/j.gca.2015.04.042

Dessert, C., Dupré, B., Gaillardet, J., François, L. M., & Allègre, C. J. (2003). Basalt weathering laws and the impact of basalt weathering on the global carbon cycle. *Chemical Geology*, *202*(3–4), 257–273. https://doi.org/10.1016/j.chemgeo.2002.10.001

Druhan, J. L., Fernandez, N., Wang, J., Dietrich, W. E., & Rempe, D. (2017). Seasonal shifts in the solute ion ratios of vadose zone rock moisture from the Eel River Critical Zone Observatory. *Acta Geochimica*, *36*(3), 385–388. https://doi.org/10.1007/s11631-017-0169-z

Fletcher, R. C., Buss, H. L., & Brantley, S. L. (2006). A spheroidal weathering model coupling porewater chemistry to soil thicknesses during steady-state denudation. *Earth and Planetary Science Letters*, *244*(1–2), 444–457. https://doi.org/10.1016/j.epsl.2006.01.055

Fuller, T. K., Perg, L. A., Willenbring, J. K., & Lepper, K. (2009). Field evidence for climate-driven changes in sediment supply leading to strath terrace formation. *Geology*, *37*(5), 467–470. https://doi.org/10.1130/G25487A.1

Gaillardet, J., Dupré, B., Louvat, P., & Allègre, C. J. (1999). Global silicate weathering and CO consumption rates deduced2 from the chemistry of large rivers. *Chemical Geology*, *159*(1–4), 3–30. https://doi.org/http://dx.doi.org/10.1016/S0009-2541(99)00031-5

Gale, J. F. W., Laubach, S. E., Olson, J. E., Eichhubl, P., & Fall, A. (2017). Natural fractures in shale: A review and new observations. *AAPG Bulletin*, *101*(8), 2165–2216. https://doi.org/10.1306/08121413151

Georg, R. B., Reynolds, B. C., Frank, M., & Halliday, A. N. (2006). Mechanisms controlling the silicon isotopic compositions of river waters. *Earth and Planetary Science Letters*, *249*(3–4), 290–306. https://doi.org/10.1016/j.epsl.2006.07.006

Georg, R. B., Reynolds, B. C., West, A. J., Burton, K. W., & Halliday, A. N. (2007). Silicon isotope variations accompanying basalt weathering in Iceland. *Earth and Planetary Science Letters*, *261*(3–4), 476–490. https://doi.org/10.1016/j.epsl.2007.07.004

Harrison, A. L., Jew, A. D., Dustin, M. K., Thomas, D. L., Joe-Wong, C. M., Bargar, J. R., … Maher, K. (2017). Element release and reaction-induced porosity alteration during shale-hydraulic fracturing fluid interactions. *Applied Geochemistry*, *82*, 47–62. https://doi.org/10.1016/j.apgeochem.2017.05.001

Hasenmueller, E. A., Gu, X., Weitzman, J. N., Adams, T. S., Stinchcomb, G. E., Eissenstat, D. M., … Kaye, J. P. (2017). Weathering of rock to regolith: The activity of deep roots in bedrock fractures. *Geoderma*, *300*, 11–31. https://doi.org/10.1016/j.geoderma.2017.03.020

Heidari, P., Li, L., Jin, L., Williams, J. Z., & Brantley, S. L. (2017). A reactive transport model for Marcellus shale weathering. *Geochimica et Cosmochimica Acta*, *217*, 421–440. https://doi.org/10.1016/j.gca.2017.08.011

Jew, A. D., Dustin, M. K., Harrison, A. L., Joe-Wong, C. M., Thomas, D. L., Maher, K., … Bargar, J. R. (2017). Impact of Organics and Carbonates on the Oxidation and Precipitation of Iron during Hydraulic Fracturing of Shale. *Energy and Fuels*, *31*(4), 3643–3658. https://doi.org/10.1021/acs.energyfuels.6b03220

Jin, L., Ravella, R., Ketchum, B., Bierman, P. R., Heaney, P., White, T., & Brantley, S. L. (2010). Mineral weathering and elemental transport during hillslope evolution at the Susquehanna/Shale Hills Critical Zone Observatory. *Geochimica et Cosmochimica Acta*, *74*(13), 3669–3691. https://doi.org/10.1016/j.gca.2010.03.036

Jung, H., & Navarre-Sitchler, A. (2018). Physical heterogeneity control on effective mineral dissolution rates. *Geochimica et Cosmochimica Acta*, *227*, 246–263. https://doi.org/10.1016/j.gca.2018.02.028

Kloprogge, J. T., Komarneni, S., & Amonette, J. E. (1999). Synthesis of smectite clay minerals: A critical review. *Clays and Clay Minerals*, *47*(5), 529–554. https://doi.org/10.1346/CCMN.1999.0470501

Maher, K. (2011). The role of fluid residence time and topographic scales in determining chemical fluxes from landscapes. *Earth and Planetary Science Letters*, *312*(1–2), 48–58. https://doi.org/10.1016/j.epsl.2011.09.040

Manna, F., Walton, K. M., Cherry, J. A., & Parker, B. L. (2017). Mechanisms of recharge in a fractured porous rock aquifer in a semi-arid region. *Journal of Hydrology*, *555*, 869–880. https://doi.org/10.1016/j.jhydrol.2017.10.060

Mayer, K. U., Frind, E. O., & Blowes, D. W. (2002). Multicomponent reactive transport modeling in variably saturated porous media using a generalized formulation for kinetically controlled reactions. *Water Resources Research*, *38*(9), 13-1-13–21. https://doi.org/10.1029/2001WR000862

Molins, S., & Mayer, K. U. (2007). Coupling between geochemical reactions and

multicomponent gas and solute transport in unsaturated media: A reactive transport modeling study. *Water Resources Research*, *43*(5), 1–16. https://doi.org/10.1029/2006WR005206

Navarre-Sitchler, A., & Brantley, S. (2007). Basalt weathering across scales. *Earth and Planetary Science Letters*, *261*(1–2), 321–334. https://doi.org/10.1016/j.epsl.2007.07.010

Navarre-Sitchler, A., Steefel, C. I., Sak, P. B., & Brantley, S. L. (2011). A reactive-transport model for weathering rind formation on basalt. *Geochimica et Cosmochimica Acta*, *75*(23), 7644–7667. https://doi.org/10.1016/j.gca.2011.09.033

Nieves-Cordones, M., Alemán, F., Martínez, V., & Rubio, F. (2014). K+uptake in plant roots. The systems involved, their regulation and parallels in other organisms. *Journal of Plant Physiology*, *171*(9), 688–695. https://doi.org/10.1016/j.jplph.2013.09.021

Ortega, O. J., Marrett, R. A., & Laubach, S. E. (2006). A scale-independent approach to fracture intensity and average spacing measurement. *AAPG Bulletin*, *90*(2), 193–208. https://doi.org/10.1306/08250505059

Pogge von Strandmann, P. A. E., Burton, K. W., James, R. H., van Calsteren, P., Gislason, S. R., & Sigfússon, B. (2008). The influence of weathering processes on riverine magnesium isotopes in a basaltic terrain. *Earth and Planetary Science Letters*, *276*(1–2), 187–197. https://doi.org/10.1016/j.epsl.2008.09.020

Pogge von Strandmann, P. A. E., Porcelli, D., James, R. H., van Calsteren, P., Schaefer, B., Cartwright, I., … Burton, K. W. (2014). Chemical weathering processes in the Great Artesian Basin: Evidence from lithium and silicon isotopes. *Earth and Planetary Science Letters*, *406*, 24–36. https://doi.org/10.1016/j.epsl.2014.09.014

Pyo, Y. J., Gierth, M., Schroeder, J. I., & Cho, M. H. (2010). High-Affinity K+ Transport in Arabidopsis: AtHAK5 and AKT1 Are Vital for Seedling Establishment and Postgermination Growth under Low-Potassium Conditions. *Plant Physiology*, *153*(2), 863–875. https://doi.org/10.1104/pp.110.154369

Reis, F. D. A. A., & Brantley, S. L. (2017). Models of transport and reaction describing weathering of fractured rock with mobile and immobile water. *Journal of Geophysical Research: Earth Surface*, 1–23. https://doi.org/10.1002/2016JF004118

Rempe, D. M., & Dietrich, W. E. (2014). A bottom-up control on fresh-bedrock topography under landscapes. *Proceedings of the National Academy of Sciences of the United States of*

America, *111*(18), 6576–6581. https://doi.org/10.1073/pnas.1404763111

Rempe, D. M., & Dietrich, W. E. (2018). Direct observations of rock moisture, a hidden component of the hydrologic cycle. *Proceedings of the National Academy of Sciences*, 201800141. https://doi.org/10.1073/pnas.1800141115

Robert J McLaughlin, S. D. E. M. C. B. J. A. S. J. W. P. I. K. R. A. G. A. C. and S. H. C. J. (2000). Geology of the Cape Mendocino, Eureka, Garberville, and Southwestern Part of the Hayfork 30 X 60 Minute Quadrangles and Adjacent Offshore Area, (April 2014), 1. Retrieved from https://pubs.usgs.gov/mf/2000/2336/ceghexpl.pdf%5Cnhttp://file//localhost(null)%5Cnpapers3://publication/uuid/E358B157-8196-432A-AB0C-3D8BE6DCF17D%5Cnpapers3://publication/uuid/07DA4042-8DCF-4D51-8BBD-7478448759C4%5Cnpapers3://publication/uuid/BF0A1765-1B

Salve, R., Rempe, D. M., & Dietrich, W. E. (2012). Rain, rock moisture dynamics, and the rapid response of perched groundwater in weathered, fractured argillite underlying a steep hillslope. *Water Resources Research*, *48*(11), 1–25. https://doi.org/10.1029/2012WR012583

Savage, D., Walker, C., Arthur, R., Rochelle, C., Oda, C., & Takase, H. (2007). Alteration of bentonite by hyperalkaline fluids: A review of the role of secondary minerals. *Physics and Chemistry of the Earth*, *32*(1–7), 287–297. https://doi.org/10.1016/j.pce.2005.08.048

Shand, P., Haria, A. H., Neal, C., Griffiths, K. J., Gooddy, D. C., Dixon, A. J., … Cunningham, J. E. (2005). Hydrochemical heterogeneity in an upland catchment: Further characterization of the spatial, temporal and depth variations in soils, streams and groundwaters of the Plynlimon forested catchment, Wales. *Hydrology and Earth System Sciences*, *9*(6), 621–644. https://doi.org/10.5194/hess-9-621-2005

Steefel, C. I., Appelo, C. A. J., Arora, B., Jacques, D., Kalbacher, T., Kolditz, O., … Yeh, G. T. (2015). Reactive transport codes for subsurface environmental simulation. *Computational Geosciences*, *19*(3), 445–478. https://doi.org/10.1007/s10596-014-9443-x

Sukhija, B. S., Reddy, D. V., Nagabhushanam, P., & Hussain, S. (2003). Recharge processes: Piston flow vs preferential flow in semi-arid aquifers of India. *Hydrogeology Journal*, *11*(3), 387–395. https://doi.org/10.1007/s10040-002-0243-3

Swoboda-Colberg, N. G., & Drever, J. I. (1993). Mineral dissolution rates in plot-scale field and laboratory experiments. *Chemical Geology*. https://doi.org/10.1016/0009-2541(93)90118-3

Van Cappellen, P., Dixit, S., & van Beusekom, J. (2002). Biogenic silica dissolution in the oceans: Reconciling experimental and field-based dissolution rates. *Global Biogeochemical Cycles*, *16*(4), 23-1-23–10. https://doi.org/10.1029/2001GB001431

Velbel, M. A. (1993). Constancy of silicate-mineral weathering-rate ratios between natural and experimental weathering: implications for hydrologic control of differences in absolute rates. *Chemical Geology*, *105*(1–3), 89–99. https://doi.org/10.1016/0009-2541(93)90120-8

Wen, H., & Li, L. (2018). An upscaled rate law for mineral dissolution in heterogeneous media: The role of time and length scales. *Geochimica et Cosmochimica Acta*, *235*, 1–20. https://doi.org/10.1016/j.gca.2018.04.024

White, A. F., & Buss, H. L. (2013). *Natural Weathering Rates of Silicate Minerals*. *Treatise on Geochemistry: Second Edition* (2nd ed., Vol. 7). Elsevier Ltd. https://doi.org/10.1016/B978-0-08-095975-7.00504-0

White, T., Brantley, S., Banwart, S., Chorover, J., Dietrich, W., Derry, L., … McDowell, B. (2015). *Chapter 2 – The Role of Critical Zone Observatories in Critical Zone Science*. *Developments in Earth Surface Processes* (Vol. 19). https://doi.org/10.1016/B978-0-444-63369-9.00002-1

Xiang, W., Si, B. C., Biswas, A., & Li, Z. (2019). Quantifying dual recharge mechanisms in deep unsaturated zone of Chinese Loess Plateau using stable isotopes. *Geoderma*, *337*(August 2018), 773–781. https://doi.org/10.1016/j.geoderma.2018.10.006